2013-09

Stratified fronts in well-mixed estuaries

Weltmer, Micah A.

Monterey, California. Naval Postgraduate School

https://hdl.handle.net/10945/37742

NAVAL
POSTGRADUATE
SCHOOL

MONTEREY, CALIFORNIA

DISSERTATION

STRATIFIED FRONTS IN WELL-MIXED ESTUARIES

by

Micah A. Weltmer

September 2013

Dissertation Supervisor: Jamie H. MacMahan

REPORT DOCUMENTATION PAGE

Form Approved OMB No. 0704-0188

1. AGENCY USE ONLY *(Leave blank)*

2. REPORT DATE
September 2013

3. REPORT TYPE AND DATES COVERED
Dissertation

4. TITLE AND SUBTITLE
STRATIFIED FRONTS IN WELL-MIXED ESTUARIES

5. FUNDING NUMBERS

6. AUTHOR(S) Micah A. Weltmer

7. PERFORMING ORGANIZATION NAME(S) AND ADDRESS(ES)
Naval Postgraduate School
Monterey, CA 93943-5000

8. PERFORMING ORGANIZATION REPORT NUMBER

9. SPONSORING /MONITORING AGENCY NAME(S) AND ADDRESS(ES)
N/A

10. SPONSORING/MONITORING AGENCY REPORT NUMBER

11. SUPPLEMENTARY NOTES The views expressed in this thesis are those of the author and do not reflect the official policy or position of the Department of Defense or the U.S. Government. IRB Protocol number ____N/A ____.

12a. DISTRIBUTION / AVAILABILITY STATEMENT
Approved for public release; distribution is unlimited

12b. DISTRIBUTION CODE

13. ABSTRACT (maximum 200 words)

The occurrence of tidal intrusion fronts in a well-mixed estuary is demonstrated through both model simulation and field observation. Strong vertical mixing in well-mixed estuaries typically does not allow for development of stratification, which is a defining feature of tidal intrusion fronts. New methodology to compute a mutual realization surface of critical width and depth from model output is described that evaluates how the geometry of a basin releases tidal inflow from the hydraulic control of an inlet and the resulting front character. Force balance relationships of these features are evaluated in three dimensions for the first time. From this, Froude angle techniques are adapted to assess and predict how the geometry controls the behavior of the front after it is formed. Intrusion fronts observed in the field do not precisely conform to the conceptual model, but a modest field validation of Froude angle usage informs an axis rotation that results in agreement with established hydraulic theory. Frontogenetic mechanisms are proposed from the observations to describe the importance of morphological complexity and water mass segregation to the occurrence of bathymetrically induced confluent subduction in a well-mixed estuary.

14. SUBJECT TERMS Physical Oceanography; estuary; tidal intrusion front; Froude number; Froude angle; frontogenesis; prediction

15. NUMBER OF PAGES
117

16. PRICE CODE

17. SECURITY CLASSIFICATION OF REPORT
Unclassified

18. SECURITY CLASSIFICATION OF THIS PAGE
Unclassified

19. SECURITY CLASSIFICATION OF ABSTRACT
Unclassified

20. LIMITATION OF ABSTRACT
UU

THIS PAGE INTENTIONALLY LEFT BLANK

STRATIFIED FRONTS IN WELL-MIXED ESTUARIES

Micah A. Weltmer
Commander, United States Navy
B.S., The Pennsylvania State University, 1996
M.S., Naval Postgraduate School, 2003

Submitted in partial fulfillment of the
requirements for the degree of

DOCTOR OF PHILOSOPHY IN PHYSICAL OCEANOGRAPHY

from the

NAVAL POSTGRADUATE SCHOOL
September 2013

Author: Micah A. Weltmer

Approved by:

Jamie H. MacMahan Professor of Oceanography Dissertation Supervisor	Thomas Herbers Professor of Oceanography
Adrianus Reniers Professor of Applied Marine Sciences	William Shaw Professor of Oceanography
Edward Thornton Professor of Oceanography (Emer.)	Thomas Murphree Professor of Meteorology

Approved by: Peter Chu, Chair, Department of Oceanography

Approved by: Douglas Moses, Vice Provost for Academic Affairs

THIS PAGE INTENTIONALLY LEFT BLANK

ABSTRACT

The occurrence of tidal intrusion fronts in a well-mixed estuary is demonstrated through both model simulation and field observation. Strong vertical mixing in well-mixed estuaries typically does not allow for development of stratification, which is a defining feature of tidal intrusion fronts. New methodology to compute a mutual realization surface of critical width and depth from model output is described that evaluates how the geometry of a basin releases tidal inflow from the hydraulic control of an inlet and the resulting front character. Force balance relationships of these features are evaluated in three dimensions for the first time. From this, Froude angle techniques are adapted to assess and predict how the geometry controls the behavior of the front after it is formed. Intrusion fronts observed in the field do not precisely conform to the conceptual model, but a modest field validation of Froude angle usage informs an axis rotation that results in agreement with established hydraulic theory. Frontogenetic mechanisms are proposed from the observations to describe the importance of morphological complexity and water mass segregation to the occurrence of bathymetrically induced confluent subduction in a well-mixed estuary.

TABLE OF CONTENTS

LIST OF FIGURES

THIS PAGE INTENTIONALLY LEFT BLANK

LIST OF TABLES

THIS PAGE INTENTIONALLY LEFT BLANK

LIST OF ACRONYMS AND ABBREVIATIONS

2D	two-dimensional
3D	three-dimensional
ADCP	acoustic doppler current profiler
ADI	alternating direction implicit
AGU	American Geophysical Union
CDOM	chromophoric dissolved organic matter
cm	centimeters
CTD	conductivity, temperature, and depth
ECSS	Estuarine, Coastal, and Shelf Science
FTLE	finite-time Lyapunov exponents
GEODAS	Geophysical Data System
GPS	Global Positioning System
Hz	hertz
ICW	Atlantic Intra-Coastal Waterway
JGR	Journal of Geophysical Research
kg	kilograms
km	kilometers
kts	knots
LCS	Lagrangian coherent structures
m	meters
MHz	megahertz
min	minutes
Mini-cat	miniature matamaran
mm	millimeters
NOAA	National Oceanic and Atmospheric Administration
NRE	New River Estuary
O( )	of the order of… (used to denote approximate magnitude)
PF	plunge front
PVC	polyvinyl choloride
psu	practical salinity unit

RIVET	River Mouth and Inlet Dynamics Experiment
s	seconds
SIPS	strain-induced periodic stratification
SWP	sea water plume
SZ	subduction zone
USACE	U.S. Army Corps of Engineers
USGS	U.S. Geological Survey
UUV	unmanned underwater vehicle
VFT	vector field topology

ACKNOWLEDGMENTS

I would like to express my sincere thanks to my supervisor, Dr. Jamie MacMahan, whose skill, expertise and guidance were critical to the success of my dissertation. His neverending quest for understanding has truly opened my eyes to the wonderful world of research, and his innovation is a model for researchers everywhere.

It has been a great privilege to have Dr. Ed Thornton as a mentor (and copy editor) during my graduate academic career. I am grateful to him for taking time out of his schedule to accompany me in the field. I quite enjoyed our philosophical discussions on the boat.

Dr. Ad Reniers' Delft3D modeling wizardry continues to astonish me. I would not have known where to even start without his assistance.

I would like to thank Dr. Tom Herbers for his sound advice and direction, and Dr. Bill Shaw and Dr. Tom Murphree for their academic support, input and counsel.

I would like to thank Professor Tim Stanton, my Master's thesis advisor, who pushed me to achieve more.

I also would like to thank Keith Wyckoff, for his ingenuity, dedication, and outstanding boatmanship.

To my fellow graduate students Jenna, Patrick, Jeanette and Casey, who loaded trucks, logged many boat hours, drove cross-country, caught a NASCAR race (Casey), and waved the Jolly Roger in triumphant pursuit of the data. I enjoyed our many hours of boat work and good conversation, and look forward to working with you all in the future.

I especially thank my Dad and Mom; your example and prayers have formed me.

Most importantly, to my lovely wife, Mona, your love and support has been unwavering for 16 years. You have carried the family these past many months, and during my absences, I owe you more than I will ever be able to repay. To my daughters, Maya and Matilda, you are my joy, my light, and my happiness. I love you.

THIS PAGE INTENTIONALLY LEFT BLANK

I. INTRODUCTION

Estuaries are important conduits between the coastal ocean and rivers for the movement of pollutants, biota, sediments, nutrients, salt, and even people and equipment (i.e., boats and swimmers). Greater than 60% of the world's population lives on or near estuaries and their associated waterways. The interaction of terrestrial and aquatic processes makes for a number of water quality and navigational safety concerns and hazards that make naval operations difficult, especially in unfamiliar or unwelcome waters. Currents can be significant and present navigational challenges; water clarity can change abruptly, stopping a diver in his tracks or increasing the risk of vessel grounding; density gradients can be intense, limiting the effectiveness of submerged vessels or the utility of a host of acoustic equipment used for mine hunting, environmental reconnaissance, force protection, and navigation. The need or desire to operate covertly or clandestinely due to expectations of hostility complicates these risks even further. Remote or autonomous sensing of fronts is an efficient means of minimizing operational risk without putting personnel into harms way.

To make sensing or modeling techniques effective, however, the hydrodynamic properties of estuarine features must be properly understood. The presence and character of estuarine fronts can offer important clues to understanding the overall hydraulic character of an estuary and the properties that control them. The exchange processes and circulation patterns that occur within estuaries are complicated and very difficult to characterize and predict, owing to relatively small time and spatial scales, limited access and data availability, variability in tidal, wave, and wind forcing and terrestrial input, and morphodynamic complexity. As a result, generalizations are frequently made based on system classification schemes, many of which have been in existence for many years. Studies typically aim to add detail to the general characterizations, adding to the temptation to make assumptions about sediment transport and contaminant pathways based on geomorphology, offshore tidal characteristics, and fresh water input that are not always valid.

This dissertation attempts to expand that paradigm. The New River Estuary (NRE) is a broad, shallow bar-built estuary on the coastal plain of North Carolina (bathymetry and nautical chart data available from NOAA Office of Coast Survey, www.charts.noaa.gov). The New River Inlet connecting the ocean to the back bay is unusually long (~3km) and narrow (~300m), and the freshwater input from the New River itself is relatively small (USGS National Water Information System, nwis.waterdata.usgs.gov). The resulting classification based on traditional methods [*Hansen and Rattray*, 1966; *Kjerfve*, 1986] is a well-mixed coastal plain estuary [*Dame et al.*, 2000] that is tidally choked (MacMahan et al., submitted to *Estuarine, Coastal and Shelf Science (ECSS),* 2013). All of these broad characterizations would lead one to believe that tides and bottom friction dominate the dynamics of the estuary, particularly when it comes to stratification (or lack thereof), fronts, and vertical mixing. This dissertation will demonstrate, however, that buoyancy and stratification can and do, under the appropriate circumstances, exert significant influence on the dynamics of such a system, resulting in a particular type of bathymetrically induced front feature called a tidal intrusion front.

Model simulations in Delft3D of idealized basins are built and evaluated in Chapter II with the intention of generating tidal intrusion fronts in a well-mixed estuary. The dimensions of the model domains follow those of the New River Estuary, and boundary inputs are imposed based on established hydraulic theory of tidal intrusion fronts [*Largier*, 1992]. The result is a well-mixed system that generates a tidal intrusion front on every cycle. The structure, evolution, and force balance relationships of the modeled fronts are described. Behavior is not exactly as current hydraulic theory would suggest, however, so these inconsistencies are explored. A new composite method of evaluating the formulae used to predict front formation is proposed that also allows interpretation of the geometric component (width or depth) that initially permits front formation. A new predictive method is also developed that uses geometric axis rotation of the non-dimensional densimetric Froude balance to describe the interaction of basin depth and width in generating and maintaining the surface fronts that do form. This material is presented here as a manuscript that will be submitted for publication in the *Journal of Geophysical Research (JGR)* of the American Geophysical Union (AGU).

Field observations of a densimetric intrusion front in the New River Estuary are presented in Chapter III. The front evaluated was a distinct surface convergence front in the lee of a shoal at the end of an artificially extended tidal channel. The front resembles a tidal intrusion front in structure, evolution, and behavior. Force balances are supercritical on both sides of the front, however, owing to its unusual confluent flow structure and oblique orientation to the primary tidal flow. The supercritical-to-subcritical transition described by hydraulic theory is obtained by calculation of cross-front balances through a field validation of the axis rotation technique developed in Chapter II. This validates the notion, simulated in Chapter II, that tidal intrusion fronts are indeed possible in well-mixed estuaries. Observations away from the front are examined to propose local mechanisms for production of a reliable supply of mid-density water and for that water to be repeatedly brought into position to allow oceanic inflow to meet with and subduct beneath it at the observed front location. Model simulations of NRE demonstrate the importance of mixing in a segregated side bay to maintaining density gradients necessary to generate the observed fronts. This study is presented as a manuscript that is also developed with the intention of submission to *JGR*.

Finally, Chapter IV summarizes the findings of this research and describes the intended direction of future work, including a second method of model-based front prediction that uses Lagrangian Coherent Structures to describe water mass boundaries.

THIS PAGE INTENTIONALLY LEFT BLANK

II. BALANCE AND CONTROL: MODEL SIMULATIONS OF TIDAL INTRUSION FRONTS IN AN IDEALIZED BASIN

A. INTRODUCTION

Tidal intrusion fronts occur when the buoyant river outflow of an estuary is blocked by a denser ocean flood tidal inflow, which then subducts beneath the fresher water and continues its advance inland as a negatively buoyant gravity current [*Armi and Farmer,* 1986; *Farmer and Armi, 1986*]. The surface convergence and associated downward plunge along the interface results in an accumulation of foam and debris that is recognizable at the surface and easily identified on remotely sensed imagery. Coincident with the foam line is a density transition, also commonly marked by turbidity or optical clarity, as the seawater encounters and displaces the ambient estuary water. The plan form of this surface expression can range from linear or irregular transverse, to concave, to a distinctive V-shape depending upon the intensity of the inflow and the geometry of the system [*Largier*, 1992]. Through study of their dynamics and generation mechanisms, tidal intrusion fronts can offer clues to the three-dimensional (3D) circulation and exchange processes of an estuary from their surface expressions alone, thereby inferring their influence on geomorphic, chemical and biological processes as well as the propagation of sound.

Tidal intrusion fronts are commonly observed in many partially mixed and salt wedge estuaries throughout the world [*Largier, 1*992; *Marmorino and Trump,* 1996; *Thain et al.,* 2004; *MacDonald and Geyer,* 2005; *Talke et al.,* 2010; *Ralston et al.,* 2010]. However, they have been neither studied nor widely reported in well-mixed estuaries. Inspection of aerial imagery, however, shows that tidal intrusion fronts appear in all types of systems. These observations underscore the importance of recognizing the limitations of global classification schemes that compare advection to diffusion [*Hansen and Rattray,* 1966]. The right combination of inflow strength, density gradient, bathymetry, and secondary circulation patterns can allow for front formation and stability in any environment.

Hydraulic theory associated with tidal intrusion fronts is well established [*Farmer and Armi,* 1986], but detailed observation efforts have only recently begun [*McDonald and Geyer,* 2005; *Talke et al.,* 2010; *Thain et al.,* 2004] and hydrodynamic model simulations do not focus on front dynamics [*Ralston et al*., 2010]. Although the numerical model studies performed to date have depicted gradients consistent with salt wedges, and by inference, intrusion fronts, this paper represents the first detailed numerical investigation of modeled fronts.

This paper evaluates the hydraulics of idealized tidal intrusion fronts in a well-mixed estuary through detailed examination of force balances (Froude numbers) and intrusion front characteristics. To accomplish this, the Deltares Delft3D-FLOW model is populated with idealized bathymetric and hydraulic boundary conditions, first to determine the capability of the model to simulate (resolve and properly depict) tidal intrusion fronts under conditions that the hydraulic theory of *Farmer and Armi* [1986] would dictate, and then to investigate the sensitivity of the development, evolution, and force balance of tidal intrusion fronts to variations in the geometry of the basin. This paper for the first time considers both the longitudinal and lateral dimensions to gain more complete insight to the modeled hydrodynamic relationships between the 3D front surfaces, the surface expressions, and inertial/buoyant force balances. A technique is proposed to evaluate threshold depths and basin widths simultaneously to determine a hydraulic control release mechanism, and adaptive 2D techniques are applied to the flows to predict the location and control mechanisms active at the fronts.

B. TIDAL INTRUSION FRONTS

Tidal intrusion fronts are created landward of a hydraulic control feature [*Farmer and Armi*, 1986; *Largier*, 1992]. The structure and flow patterns associated with an idealized tidal intrusion front are shown in Figure 1 (found in the FIGURES section following Chapter IV). As the dense inflow passes through a constriction or over a sill acting as a control structure, the velocity is enhanced, arresting the buoyant outflow in the lee of the control feature. A surface front, considered a hydraulic jump in this context, forms where the expansion of the flow decreases the velocity into balance with the relative buoyancy of the water masses. The dense inflow then subducts beneath the buoyant outflow and continues its upstream advance as a densimetric gravity current [*Largier*, 1992; *Lowe et al.*, 2002; *Gristenko and Chubarenko*, 2010].

The subsurface structure of a tidal intrusion front (Figure 1a) has a characteristic stratification that persists through the life cycle of the surface front because mixing is not efficient across intrusion fronts. The surface-based subduction zone and "toe" of the densimetric intrusion (each labeled in Figure 1) are considered the active elements of the front, with the stratified region between the two ends supporting the advance of the gravity current by suppressing the vertical mixing [*Largier*, 1992; *Giddings et al.,* 2012]. In more rapidly advancing gravity intrusions, laboratory experiments have shown the middle stratified portion to form dissipative billows that weaken the stratification slightly [*Lowe et al.,* 2002; *Gristenko and Chubarenko*, 2010]. The same studies also showed these billows to form on the lateral margins of the intrusion, and could serve in this setting as a precursor to eventual dissipation of the front as the flood progresses landward and hydraulically decouples from the control structure.

Tidal intrusion fronts are often hydraulically "anchored" to the bathymetric control feature inducing it, resulting in a concave or V-shape (as depicted in Figure 1b) due to the strength of the central flow [*Marmorino and Trump*, 1996; *Thain et al.*, 2004]. Post-formation advancement has also been observed [*Marmorino and Trump*, 1996; *Talke et al.*, 2010; *Thain et al.*, 2004], and though sometimes the front physically detaches from the shoreline, maintenance of the front relies upon remaining dynamically rooted to the hydraulic control structure. Studies have shown that tidal intrusion fronts can therefore be relatively short lived, persisting for as little as 2-3 hours until the density gradients advance beyond the hydraulic influence of the constriction or sill [*Thain et al.*, 2004].

Tidal intrusion fronts are common around the world in moderately forced partially-mixed estuaries where the freshwater outflow matches the tidal forcing [*Largier*, 1992; *Marmorino and Trump,* 1996; *Thain et al.,* 2004; *Talke et al.,* 2010; *Ralston et al.,* 2010]. In strongly forced salt wedge estuaries, such as the Columbia [*Jay and Smith*, 1990], Fraser [*Geyer and Farmer*, 1989; *MacDonald and Geyer,* 2005], Snohomish

[*Wang et al.,* 2009] and Merrimack [*Ralson et al*., 2010] Rivers, a persistently stratified salt wedge develops that propagates up and down the estuary with the tidal fluctuations. The structure, circulation patterns, force balances, and upstream advance of the salt wedge during flood tides may all resemble those of a tidal intrusion front, but it is technically distinguished from a tidal intrusion front if it is not hydraulically linked to a bathymetric control feature. To date, tidal intrusion fronts have yet to be documented in any wide, shallow estuaries that are classified as well-mixed, owing to their definition as a stratification feature and the implied balance between tidal and fresh water forcing.

Tidal intrusion fronts are evaluated by comparing the characteristic fluid velocity to gravity wave celerity via the Froude number (Figure 1, blue line at top), a non-dimensional ratio of the inertial forcing to buoyancy forcing. Where the inertia dominates the system (F>1, "seawater plume" in Figure 1), the dense inflow will displace the buoyant outflow; stratification will occur where buoyancy is greater (F<1, "intrusion zone"). The surface convergence front occurs at the point where the two forcing terms come into balance (F=1, "plunge front"). Vertical shear between the layers typically opposes one another, reducing the characteristic velocity in a depth-averaged sense and ensuring the intrusion zone remains subcritical.

For an estuary-inlet system, *Farmer and Armi* [1986] define an Input Froude number F_0^2

$$F_0^2 = \frac{Q_0^2}{g' h_0^3 b_0^2} \tag{1}$$

to evaluate the force balance at the inlet, where $Q_0 = u_0 h_0 b_0$ is the volume flux from the ocean into the estuary, g' is gravity normalized by the fractional density difference between estuary and ocean, $g' = g\frac{\Delta\rho}{\rho_0}$, h_0 and b_0 are the water depth and channel width and u_0 is the depth averaged velocity, all defined at the tightest constriction within the inlet. Subcritical inflow ($F_0^2 < 0.3$) will flow into the estuary strictly at the subsurface, while the estuary water continues its seaward outflow at the surface. In the transitional regime ($0.3 < F_0^2 < 1$) the intruding ocean water partially blocks the seaward flow, but cannot prevent it from entering the inlet entirely. A surface front is generated within the inlet seaward of the control point, but only temporarily as this is strictly a transitional state. When supercritical ($F_0^2 > 1$, depicted in Figure 1), the flood flow has established control of the inlet, blocking any buoyant outflow from entering the inlet.

Once the ocean inflow has reached a basin cross-section sufficient to accommodate a buoyant layer in addition to the inflow's volume flux Q_0, an intrusion front may form within the back bay at a location stabilized by the geometry of the basin. The controlling inflow becomes subcritical and continues its up-estuary advance by subducting beneath the buoyant estuarine water mass. The location where this is predicted to occur, as a result of attaining either a critical width ($b=b_p$) or depth ($h=h_p$), is called the plunge point and is described analytically [*Farmer and Armi,* 1986] by

$$h_p = \left(\frac{Q_0^2}{g'b^2} \right)^{\frac{1}{3}} \tag{2}$$

$$b_p = \frac{Q_0}{\left(g'h^3\right)^{\frac{1}{2}}} . \tag{3}$$

The basic hydraulic control state of a 2-layer fluid system at any given location and time is described by its densimetric Froude number,

$$F^2 = \frac{\left|u_d\right|^2}{g'h} \tag{4}$$

where u_d is the depth-averaged horizontal velocity and h is the depth of the water column. The transition from supercritical ($F^2>1$) to subcritical ($F^2<1$) is often abrupt and associated with a hydraulic jump. In the case of tidal intrusions (Figure 1), the hydraulic jump manifests as a surface convergence front ("plunge front" in Figure 1), but the full nature of the front is described by the details of the more complete Froude analysis described here. For more complete consideration of a 2-layer system, *Farmer and Armi* [1986] define a Composite Froude number

$$G^2 = F_1^2 + F_2^2 \tag{5}$$

where the layers F_1^2 and F_2^2 are evaluated independently in the form

$$F_i^2 = \frac{|u|_i^2}{g' h_i}. \tag{6}$$

Calculation of G^2 allows expansion of the definition of "critical" from a single point ($G^2 = 1$) where the hydraulic jump occurs to a range of "transcritical" values ($0.3 < G^2 < 1$) to describe the full extent of the stratification zone [*Largier*, 1992]. *Thain et al.* [2004] found limited value in G^2, and instead determined the Mixing Froude number, F_Δ^2, to be a more reliable indicator of surface convergence front location. F_Δ^2 describes the stability of the vertical interface between water masses, and is evaluated as

$$F_\Delta^2 = \frac{|\vec{u}_1 - \vec{u}_2|^2}{g' h} \tag{7}$$

where $|\vec{u}_1 - \vec{u}_2|$ is the vector shear between layers [*Largier*, 1992]. $F_\Delta^2 < 1$ describes an interface that is mixing weakly or not at all, while $F_\Delta^2 > 1$ indicates significant mixing that is expected to weaken or entirely break down the water mass boundary.

In nature, however, the one-dimensional flows used to derive the balances described above are rarely observed. *Largier* [1992] describes a conceptual classification scheme for 2D flows, but explicit treatment of 2D flows is not well documented for tidal intrusion fronts. Section E will discuss techniques developed and tested for ebb tidal lift-off or plume fronts [*Garvine*, 1982; *O'Donnell and Garvine,* 1983; *O'Donnell,* 1990; *MacDonald and Geyer,* 2005] and their adaptation for prediction of tidal intrusion fronts.

C. METHODS

1. Numerical Model Formulation

Numerical simulations are conducted in Delft3D, a multi-dimensional software suite that is capable of integrating simulations of flows, sediment transport, waves, water quality, morphological development and ecology for coastal, river or estuarine settings [*Deltares,* 2010]. The Delft3D momentum and transport formulations have been extensively validated in the laboratory (as summarized in [*Lesser et al.,* 2004]). Field validations have demonstrated the utility of the various Delft3D components for shallow water applications ranging from nearshore hydrodynamics and morphodynamics [*Morris,* 2001; *Hsu et al.,* 2008; *Reniers et al.*, 2009] to estuarine wave and wave-flow coupling [*Mulligan et al.,* 2008, 2010] and plume dynamics [*Mulligan et al.,* 2011].

The hydrodynamic and transport simulation module of Delft3D is called Delft3D-FLOW. This module solves the nonlinear shallow water system of equations in 2D (depth-averaged) or 3D. Gravity is assumed to be the dominant vertical forcing term, reducing the vertical momentum equation to the hydrostatic pressure relation; vertical velocity is driven by continuity. Delft3D-FLOW is thus well suited for shallow water applications, where horizontal momentum and phenomena are of much greater magnitude than those in the vertical. Horizontal pressures are treated with the Boussinesq approximation, and Reynolds stresses use eddy viscosity and diffusion with a selectable implementation of turbulence closure models. Bottoms are no-slip, but drag calculation is selectable. Lateral boundaries are free-slip if closed, and open boundaries are user-defined, with waterborne constituent inputs also defined at the open boundaries. Although other constituents are available, salinity is the lone active constituent calculation used here, since it is the most dominant contributor to density variations in the estuarine environment.

Numerically, Delft3D is solved as finite differences in an "Arakawa C" staggered grid configuration. *Alternating Direction Implicit (ADI)* time integration, which splits the time step into two half-steps, is employed to ease time step restrictions. This allows for Courant numbers up to $4\sqrt{2}$ where grid lines do not follow topography well, or further relaxation to O(10) in most other practical situations. The horizontal discretization scheme for both advection and transport is *Cyclic*, which uses the sum of a 2nd order central difference scheme and a 3rd order upwind scheme to achieve 4th order accuracy. Vertical discretization is a simple 2nd order central difference. Eddy viscosity and diffusivity and 3D turbulence closure schemes are all fully user defined.

2. Numerical Model Domains

The possibility of tidal intrusion fronts in well-mixed estuaries is not well documented, or even emphasized, in the literature. Inspection of aerial imagery, however, reveals that some well-mixed estuaries, such as the lower New River Estuary (NRE – Figure 2a), NC, do generate V-shaped tidal intrusion fronts in certain circumstances (Figure 2b). The appearance of tidal intrusion fronts in this particular well-mixed system, along with the dynamic separation between the ocean and back bay created by the long, narrow inlet, make the NRE an optimal location to expand the study of tidal intrusion fronts. A subsequent multi-institutional field campaign at this site enables testing of general conclusions from this study under real-world conditions. Thus, the NRE system is emulated in this study's idealized geometry.

A series of model domains were constructed and scaled corresponding to the NRE to examine dynamic sensitivities to basin geometry. One was designated the baseline, from which basin width and bathymetry were systematically altered and analysis algorithms run to compare results. The geometric variations examined in this study are shown in Figure 3. The baseline basin shape (Figure 3a, thick black outline) is also referred to within this study as "open". Variation is introduced by creating an alternate set of geometries that retains the overall characteristics of the "open" set, with the exception that it narrows the basin by 50% (Figure 3a, dashed magenta line), referred to as the "narrow" type. The bathymetry of each domain is symmetrical about the longitudinal axis, dropping sharply from 2 m above mean water level to 1.5 m below to define the margins of the basin, then sloping linearly toward the axial bathymetry profile. This central profile is then altered as shown in Figure 3b to impose the bathymetric variation between domains. In the baseline case ("baseline", solid black), the axial profile remains flat at 1.5m as it enters the basin to allow the effects of basin widening to dominate. The gradual widening of each basin type allows for precise determination of basin width. Approximately 1km into the basin (X=4500m), the depth increases at a moderate slope to 3.5m, where it again flattens until sloping back up to the 1.5m deep river entrance. The second axial profile ("shallow", dashed blue) reduces the slope by a factor of 2, but is otherwise identical to the first profile. The third profile variation ("close", dashed red) retains the slope of the baseline, but pulls the slope break back almost immediately adjacent the inlet (X=5500), allowing the depth and width to synchronously affect the flow dynamics.

The model domain has two open boundaries, representing the river input and the oceanic forcing. The river boundary is 250m wide by 1.5m deep, and is labeled in Figure 3a as segment (A) partially defining the basin wall. The ocean (not shown) is connected to the basin by a 3000 m long inlet, which is 375 m wide and 1.5m deep at its narrowest point (B in Figure 3a) and gradually grows to 500 m wide and 3 m deep at its mouth. From the linear shoreline at x~8500 m, the ocean portion of the domain slopes linearly to 10 m water depth at the open ocean boundary located at x=10,000 m, some 4000 m beyond the right hand side of Figure 3a. The geometry of the river boundary, inlet, and ocean boundary remain constant, ensuring only the sensitivity to the basin geometry is considered.

Each domain is constructed of a rectilinear 25 m grid to ensure important features, in particular the inlet, are adequately defined by a minimum of 10*Δx* [*Roelvink and Reniers,* 2011]. Since vertical motion is a necessary component of tidal intrusion front dynamics, ten sigma layers are defined in an upward-increasing proportion of total water depth from 2% in the bottom layer to 20% in the top (surface) layer. The effects of the earth's rotation are not considered. Each simulation is run at a 10 minute time step for 30 days to ensure a dynamic equilibrium state is attained. Courant numbers for these simulations max out at ~12 at the inlet control point during the tidal flood and decrease rapidly as velocities decrease away from the constriction. This falls within Delft3D-FLOW's recommended O(10) Courant number limit [*Deltares*, 2010] and allows for stable results and meaningful qualitative comparisons of tidal intrusion fronts dynamics.

Classification of exchange properties for each of the idealized domains is determined by plotting a cloud of points representing each grid point in stratification-circulation space [*Hansen and Rattray,* 1966]. The stratification parameter is defined as the ratio of the top-to-bottom salinity gradient to the average salinity of the section, $\delta S/S_0$, and the circulation parameter relates the local surface velocity to the total fresh water (seaward) velocity of the section, u_s/U_f, to determine the relative contribution of advection compared to diffusion to the overall salt transport of the estuary. This method indicates that stratification everywhere is slight and that diffusive transport dominates over advective transport in most places, but not all. Like the NRE, the idealized estuaries in this study would thus be considered well-mixed, though some consideration must be given for partial mixing processes to occur [*Hansen and Rattray*, 1966].

3. Physical Parameters and Boundary Forcing

Eddy mixing coefficients are calculated using a *k*-L 3D turbulent closure scheme, with background values (both viscosity and diffusivity) set to $1e^{-1}$ in the horizontal, and vertically to $1e^{-6}$ for diffusivity and $5e^{-5}$ for viscosity. Keeping this arrangement minimizes eddy dispersion and allows advective processes to be explicitly modeled, as long as model stability permits [*Geyer and Signell,* 1992; *Hench and Leuttich,* 2003]. It also ensures that horizontal mixing processes dominate over vertical processes. Bottom roughness is modeled with z_0=10 cm to account for large bed forms generated by mobile sediment, but similar results can be obtained with a Manning formulation if a shorter time step (i.e., 1 minute) is used.

The offshore boundary is forced by the semidiurnal (M_2) tide with amplitude of 0.5 m for all runs to correspond to the dominant forcing offshore of the New River Estuary. Reflected energy above tidal frequencies was permitted to pass out of the domain without re-reflecting or destabilizing the boundary. Thatcher-Harleman time lag, or return time, was set to allow salinity inputs to begin at the value of the outflow and recover to the defined boundary salinity over a 60 minute period.

The river boundary is considered to represent the values for the backbay as a whole for the idealized simulations of this study. Super-elevation, Δ, an elevated mean water level of the bay due to riverine input, is simulated in the model as a positive mean water level offset at the river boundary. Extension of the tidal signal beyond the open river boundary is simulated with a dampened semidiurnal tide at the river boundary, M_{2b}. M_{2b} and Δ, summarized in Table 1 (TABLES section following Chapter IV), are kept as high as possible to retain the greatest possible forcing to the system but selected to ensure the salinity gradients dynamically stabilize in the portion of the basin that best supports intrusion front formation. The dampened semidiurnal forcing, quantified in Table 1 as M_{2b}/M_{2o}, and significant phase lag (α) are consistent with analytical models of tidal response in back bays [*Keulegan*, 1967; *King*, 1974]. The along-stream location and magnitude of the tidal excursion were, in fact, found to be highly sensitive to these variations, and adjustments in M_{2b} of less than 1 mm or 0.5° in some cases prevented the salinity gradients from achieving a dynamically stable location within the basin.

Salinity at the open river boundary is assigned from the plunge point predictions of *Farmer and Armi* [1986], given in Eqs. 2 and 3. These equations are solved for the threshold density difference using the depth of the sill and maximum basin width, which is then converted to ΔS (Table 1). Since plunge width is inversely proportional to the depth in these calculations, assigning the salinity in this manner ensures that the initial subduction of the deep basins considered in this study are reliably located between the inlet and the point at which the basin reaches its maximum width, approximately 2 km from the inlet. From a uniform initial condition of S_0=34 psu, the salinity at the river boundary is drawn down linearly such that it attains its final state, $S=S_0-\Delta S$, at the start of the 10th simulation day. Each domain is then allowed to run for 5 additional days to establish dynamic equilibrium before analysis is performed on the output.

4. Model Validation and Sensitivity

"Validation" is considered by qualitatively verifying the appearance of a tidal intrusion front. Initial tests conducted in a flat basin were successful in verifying the capability of Delft3D to properly resolve and depict stable tidal intrusion fronts under analytically appropriate hydraulic and densimetric conditions. Included in the discriminating features are subduction and advance of the dense ocean water gravity current beneath the more buoyant estuary water, predictable surface front locations with consistent relationships to the basin features and stratification that persists through the tidal cycle, and Froude balance transitions from supercritical to subcritical that qualitatively match the front locations. As a sensitivity check, results are compared when salinity depression is reduced by just 0.5 psu. The inverse relationship between b_p and ΔS (Eq. 3) places the predicted plunge location at a physically unrealistic basin width (wider than the model basin) and tidal straining results. An equal increase in the salinity depression slightly alters the location of the fronts, which remain otherwise unaffected. It is concluded from these results that Delft3D-FLOW correctly simulates tidal convergence and mixing regimes appropriate to the basin geometry and densimetric inputs. Further sensitivity analysis to bathymetric boundaries is examined in the results section of this paper.

D. RESULTS

Tidal intrusion front features are analyzed and force balances are calculated over the entire model domain for one complete semidiurnal tidal cycle. Froude numbers are calculated at each time step for all grid cells using Eqs. 1-7 above. Reduced gravity g' is calculated using the total vertical range of water density at each grid point, and depth-averaged velocity (v_{dav}) is weighted by fractional thickness of the σ layers. Where two vertically stacked water masses are present, the interface at each grid point is calculated as the bottom of the layer within which the central difference of the total vertical density range falls. Surface layer ($\sigma 1$) velocity is taken to represent the top water mass, and the highest model layer beneath the transition characterizes the bottom water mass. Where two water masses are not present, the Froude number of the absent water mass is not calculated, but F_{Δ}^{2} (Eq. 7) is converted to a near-surface gradient value using the vertical shear between the $\sigma 1$ and $\sigma 3$ layers. All velocities are calculated as total vectors, including $\left|\vec{u}_1 - \vec{u}_2\right|$ for calculation of F_{Δ}^{2}, to allow hydraulic analyses of both the streamwise and transverse dimensions.

Three phases of the semidiurnal tidal cycle are used to identify salient features of the intrusive process (Figure 4, vertical lines). The phases examined for each model run are referenced to tidal low water (t=0) at the inlet: T1) after the inflow becomes controlled but before the tidal elevation reaches zero (t=2 1/3 hours, blue line); T2) the mid-point between zero elevation and maximum hydraulic control (t=3 2/3 hours, green line); and T3) at maximum hydraulic control state (t=4 2/3 hours), after which front stability begins to degrade. F_{0}^{2} and elevation (Figure 4, black and magenta curves, respectively) are calculated at the center of the minimum inlet cross section (the control point), and given directionality using the form

$$F_0^2 = \frac{Q_0 \left| Q_0 \right|}{g' h_0^3 b_0^2}. \tag{8}$$

where Q_0 is positive into the basin, and g' in this particular case is calculated using the density extremes at the boundary inputs (Table 1). F_0^2 (Figure 4, black curve) leads the tidal elevation (magenta curve) by just 70-80 minutes, indicating a distinct progressive vice reflective tidal wave signature. This is due to the highly dissipative and weakly reflective characteristics of the long, shallow inlet and backbay [*Hench and Leuttich,* 2003; *Friedrichs,* 2010].

T1 marks the shift of hydraulic control state from river to inlet dominance for the basin. For approximately 1 hour prior to T1, the rising ocean tide impedes the river outflow through the inlet, resulting in convergence, and therefore fronts, within the estuary. The river is still flowing into the basin, effectively enhancing the total control state within the basin (inlet + river inputs, Figure 4, gray dashed curve). After T1, the river input is quickly extinguished, as the entire estuary transitions to flood flow. With near zero input from the river at T2, the inlet (Figure 4, black curve) exerts exclusive influence over the total control state. By T3, F_0^2 at the river flow has turned upstream, weakening the total control state of the back bay slightly from what would be predicted by the inlet alone, although both inlet and total hydraulic control are near their maximum at this phase.

The tidal intrusion fronts generated in these simulations form every tidal cycle within 30 minutes of the flood flow reversal within the inlet as the inflow plume reaches the bathymetry break, where it subducts beneath the buoyant estuary water and continues its advance up the estuary as a gravity current flowing down the slope. The features associated with the front, labeled in the idealized front structure (Figure 1), are the plunge front, subduction zone, seawater plume, and the pycnocline. The plunge front (PF) is the analytically identified surface front feature. The surface convergence front manifests best in the model as downward surface (*σ1*) velocity, so PF location is evaluated as downward velocities greater than 0.01 cm/s ($\vec{w} \le -0.01$cm/s, Figure 5a). Comparison of the PF with the leading edge of the seawater plume (SWP), evaluated in the model as the reduction of the surface (buoyant) layer to zero thickness (Figure 5b) shows agreement to within 1 or 2 grid cells (see overlapping contours in Figure 5b), or 50 m, in every model run within 30 minutes of the transition to flood tide. The subsurface propagation of downward velocities from the PF to the subsurface gravity current is termed the subduction zone (SZ). The two features are defined identically and differentiated only in that the PF is a surface only feature, and the SZ is three-dimensional. Similarly, using the pycnocline, or the density gradient based division between the dense and buoyant layers, to define the full 3D tidal intrusion front surface makes it the 3D expression of the surface-only SWP.

The river boundary initially continues to input less saline water to the estuary, forcing a seaward flow at the surface and helping to generate the front. As the gravity current advances, the tidal wave propagates through the estuary to the river, turning its flow upstream. The surface flows weaken, but the advance of the surface front and gravity current continues up-estuary until the peak flood flow (~T3), after which the convergence and subduction weaken and begin to allow vertical mixing that degrades the stratification.

1. Horizontal Structure and Evolution

PF evolution for each basin geometry combination (Figure 3) over the evaluated time steps (Figure 4) is shown in Figure 6. In each case, the PF appears at T1 (blue arrowheads) as a 400 m wide crescent shape centered in the basin. The initial location of the baseline case (Figure 6a) reaches ~1400 meters into the basin from the control point, although individual simulations range from ~1000 meters (narrow close case, Figure 6f) to more than 1600 meters (open shallow case, Figure 6b) into the basin. Variation among cases in shape, width, and advance rate are much more substantial at subsequent times. In the baseline bathymetry (Figure 6a), but not in any other case, downward surface motion appears above the bathymetric break (x~4500) and persists through the flood tide. By T2 the PF has advanced around 500 m and doubled in width to 800m (green arrowheads, Figure 6a). The shape flattens near the centerline, with a 300 m wide central segment and offset lateral portions that are slightly advanced relative to the center section (green arrowheads, Figure 6a). This PF offset is accentuated at T3 (cyan arrowheads, Figure 6a), with the central 300 m portion now trailing the laterals by 100 m. The flattened central section has advanced ~200 m more, while the lateral offset portions have advanced laterally as well, causing the entire front to expand another 200 m to nearly 1000 m wide (Figure 6a). Dissipation observed in the laboratory [*Lowe et al.*, 2002; *Gristenko and Chubarenko*, 2010] along the lateral margins of densimetric intrusions may explain the processes that are limiting the PF width to only the actively advancing forward edge of the SWP.

a. Shallow Slopes

Easing the slope of the bathymetry after the same slope break location does not notably impact the hydraulic control of the system. F_0^2 magnitude is ~10% greater than for the baseline case, but relationships between and among the inlet and river control inputs are otherwise nearly identical.

The plunge front shape of the shallow slope case is similar to the baseline case (compare Figure 6b with 6a). The most noticeable difference is the rounding of the plunge front observed at all evaluated time steps (Figure 6b). The initial plunge occurs slightly farther into the back bay, but the subsequent advance rate is identical to that of the baseline case. The shallow slope generates a wider PF at T2 and T3 (green and cyan arrowheads). An unusual three-lobe PF expression also emerges at T3 (cyan arrowheads, Figure 6b). Force balance transitions are much more abrupt between the lobes (not shown), possibly signaling some sort of dynamic shift is occurring between lobes.

b. Closer Bathymetric Break

A bathymetric break location closer to the inlet results in substantial changes to the flows, structures, and interfaces (Figure 6c). Although the PF starts closer to the inlet (see blue arrowheads at x~4500) as expected due to the shifted bathymetric break, it advances more rapidly from T1 to T2 (blue to green) than in any other case studied, advancing beyond even the T3 (cyan) position of the distant slope cases (compare Figure 6c to Figures 6a,b). From T2 to T3 the advance slows, but still outpaces either of the previous cases. The shape of this front is V-shaped throughout the flood, and the width of the plume is reduced by 50% compared to the distant slope cases, expanding only narrowly beyond the width of the inlet. Together these factors indicate a more intense longitudinal flow, a conclusion supported by 20% greater magnitudes in F_0^2 (not shown). Increased flows also push the SWP farther into the back bay for this case, almost twice as far as the PF at T1 (not shown). The PF advances rapidly, but by T2 has still not caught up to the leading edge of the SWP. By T3, the advance of the plume slows, allowing the front to finally catch up, stabilize and expand laterally.

c. Narrow Basins

The initial front locations and advance rates in a narrow basin are remarkably comparable to those in the open basin type, but patterns in the plunge front shape and evolution appear more sensitive to variations in the bathymetry (Figure 6d-f). Narrowing the basin requires an increase in the salinity depression to -8 psu to satisfy Eqs. 2-3 and achieve intrusion front formation. The tighter longitudinal gradients result in more compressed structures (not shown). The subduction zone is very steep but extends deeper, and a thin but intense stratification persists throughout the tidal cycle in the deepest parts of the basin. Turbulent dissipation is observed along the top of the residual stratification that greatly complicates analysis of the subsurface intrusion. The reduced basin width also meant that the SWP rapidly expanded to the full width of the basin (see green and cyan arrowheads in Figure 6d,e). This limits the analysis of the narrow basins to the longitudinal dimension, and if viewed as an analogue to a river mouth estuary, helps to explain the limited scope of previous intrusion front investigations to the longitudinal dimension. Because of these complications and limitations, the full narrow basin analysis results are not discussed further.

2. Horizontal Force Balance Relationships

PF evolution of the baseline case is compared to several Froude balance patterns in Figure 7. The top row shows the spatial evolution of the depth-averaged Froude number (F^2) that forms the basic hydraulic control state of the water column. The middle row depicts the mixing Froude number (F_Δ^2), which was found by *Thain et al*. [2004] to be the most reliable determinant of intrusion front location. The last row shows the Composite Froude number, which has been used extensively to discuss the 2-layer hydraulics of an intrusion front [*Farmer and Armi*, 1986; *Largier*, 1992]. In addition to comparisons in PF alignment, gradients and patterns are described that may help to explain some of the behavior of the fronts.

Depth-averaged Froude numbers, F^2, describing the general extent of the inlet forcing into the back bay (Figure 7a,d,h), fall from supercritical to critical very close to the PF location (red/yellow boundary). During the first half hour of flood transition (T1, Figure 7a), however, the PF occurs entirely within the supercritical (red) region. At T2 andT3, the ends of the PF, where it is aligned more obliquely to the longitudinal flow, slide entirely into the supercritical region (x,y=3800,500 m, Figure 7d,h). In this instance, F^2 could be an indicator of frontal activity. F^2 is supercritical at the T1 PF (Figure 7a, near centerline). This is certainly where the primary subduction is occurring, since the PF at this point is still advancing to reach its dynamic stability position. At T2 and T3 (Figure 7d,h), the PF falls into the supercritical regions of F^2 in the off-center regions (y~+/- 300 m) where the PF has not yet stalled and flattened, but has expanded laterally. The suggestion is that F^2 is supercritical at PF locations where front-normal forcing components are sustaining SZ activity and lateral expansion. Conversely, in locations where the PF occurs at the critical F^2 transition, flow (and hence forcing) is either deflected parallel to the front or diminished, limiting expansion at those locations.

Mixing Froude number, F_Δ^2, shows a narrow rise into the critical range along much of the margin of the SWP, coinciding in most cases with the PF location (Figure 7b,e,h). The tongue of shear-induced mixing that emerges from the inlet (“supercritical” region near the centerline, x>4000) is an interesting feature that appears due to the calculations performed where only the dense layer is present. It is initially confined to the width of the constriction and quiets quickly after passing the bathymetric break to a more laminar (low-shear) flow. Interestingly, the shear spikes and F_Δ^2 becomes critical at the surface plunge (Figure 7b), making it the only balance to show a critical transition coinciding with the PF at T1. At T2, the tongue has expanded 50% beyond the width of the inlet and more than 500 m beyond the bathymetric break, although the flow does still become more laminar prior to rising to critical near the SWP edge (Figure 7e). By T3 (Figure 7h), the tongue has extended farther into the basin, but low mixing zones encroach laterally into the supercritical tongue, perhaps an artifact of lateral dissipation.

The composite Froude number G^2 is supercritical nearly everywhere within the SWP and intrusion zone (Figure 7c,f,i), including the PF location and beyond. This indicates deep layer dominance since the buoyant layer Froude numbers fall quickly to subcritical (not shown). The 3-lobed appearance of G^2 may indicate enhanced secondary circulation, but otherwise shows little relationship to the position of the surface front.

Overall, the best determinant of surface front location is F^2. It may have supplemental use in determining which parts of a front are actively advancing, and the width of the transcritical region appears modest enough to perhaps correspond to a subsurface feature. F_{Δ}^2 appears to align well with the PF at all evaluated times, but its requirement for 2 layers in its computation significantly limits widespread utility. Further, the alignment at T1 is artificial in that the balance was computed in this vicinity only as a shear proxy; 2-layer stratification was *not* present. G^2, despite widespread use in the development of hydraulic theory, does not show any useful relationship to PF location.

3. Subsurface Structure and Evolution

a. Longitudinal Profiles

The colored density contours in Figure 8 indicate barotropic flow exiting the inlet and transitioning to 2-layer stratification at the SWP edge. The water mass boundary is qualitatively estimated as the contour dividing the yellow and light green shaded regions. Coincident with this transition is the downward turn of the velocity vectors indicative of the PF. The exception is T1 (Figure 8a), when the PF appears ~100 m prior to reaching the edge of the SWP (near the yellow/orange contour). The closely spaced density contours of the pycnocline (greens and yellows) initially slope more steeply from the surface to ~1 m to mark the SZ, which then joins with a residual deep stratification as the pycnocline flattens out. Some distance (x=3500m at T1, x=2500m at

T2, x=2000 by T3) up-estuary of the SZ, the pycnocline steepens again and the velocities show an upward turn. Herein referred to as the toe, this feature represents the leading edge of the gravity current, and is consistently observed, but only in longitudinal profiles where an active PF and SZ are present. Velocities throughout the deep layer are up-estuary, slowing at and beyond the toe to match its advance speed. This is consistent with laboratory observations that describe horizontal velocities in the "tail" of an intrusive gravity current 20-30% higher than those at the energy-conserving toe region [*Lowe et al.*, 2002; *Gristenko and Chubarenko*, 2010]. The toe is contained laterally to the width of the active plunge front, and outboard of this, the residual pycnocline deepens landward more linearly (not shown).

When the PF and SZ initially form near the bathymetric break, they are difficult to distinguish from the downslope current (Figure 8a) and not aligned with the main surface density gradient. As the PF advances, the downward velocities of the SZ are more distinguishable from those of the downslope current because of the separation (Figure 8b). The PF lines up with the density gradients, and the SZ with the now steeper pycnocline. These alignments continue at T3 (Figure 8c), as does the steepening of the pycnocline, which may indicate a local increase in vertical mixing as PF and SZ advance slows. Generation of the downslope gravity current is the primary frontogenesis mechanism of tidal intrusion fronts [*Largier*, 1992]. However, the gravity current appears to remain rooted at the slope break but advances more rapidly than the PF and SZ. This may indicate a decoupling of these features that could warrant independent consideration in future evaluations, particularly where a residual deep stratification is present.

The colored shapes plotted above the profiles show the various Froude numbers calculated along the respective profile to compare these analytical predictors to the actual velocity and density features. The first observation is that F^2 and F_Δ^2 both transition from supercritical to critical (dotted red lines in Figure 8 are $F=1$) very close to the surface expression of the pycnocline (the SWP edge) and the PF (downward surface velocities). The lone exception is F_Δ^2 at T1, which transitions at x=4300 and is the only Froude transition aligned with the PF at this time (see also Figure 7b). The critical to subcritical transition (green dotted lines are $F=0.3$) of both F^2 also aligns with a transition of the pycnocline from the SZ to the gravity current. Hence, the relative steepness of F^2 corresponds to that of the SZ, and is nearly instantaneous where no plunge front exists, as will be seen in the next section, e.g. along the lateral margins of the plume (see Figure 9). These results seem to suggest multiple processes at work in the SZ to differentiate it from the main gravity current. No clear pattern is discernible in the decrease of G^2 from supercritical to critical levels (Figure 8).

b. Lateral Profiles

Previously not emphasized in the literature, the lateral subsurface structure of tidal intrusion fronts is examined in Figure 9. In this dimension, particularly in the narrow basin simulations, frontogenesis appears to occur more as a result of surface-convergent lateral circulation cells resembling those described by *Nunes and Simpson* [1985], but separated in the center by the advancing SWP. Pycnoclines are easily identified as in the longitudinal profiles, and are observed to lifted up and outward by the advancing seawater intrusion (compare in the sequence of Figure 9a,b,c). Up-estuary velocities show subsurface maxima coincident with the bottom of the pycnocline (yellow/light green contour) in advance of the plunge front (Figure 9a), consistent with a change in dynamics between layers. Lateral transitions in the pycnocline depth are observed, but much less dramatically since this is not the principal flow direction. Length scales of the intrusion zone in the lateral dimension are 100-200 m, from the plunge front to the subsurface limit of expansion. The pycnocline transition is accompanied by horizontal density and up-estuary velocity gradients in the deep layer, clearly marking the lateral limit of the seawater intrusion and highly suggestive of the baroclinic forcing that would be more prominent in this dimension [*Giddings et al.*, 2012].

Froude balances in the lateral dimension (plotted above the density contours in Figure 9) reveals in all cases relationships with the density and velocity structures equivalent to those in the longitudinal dimension (Figure 8). The differences in length and density gradient scales, which are both up to an order of magnitude smaller, are the only major distinctions in evaluating these relationships. F^2 declines through transcritical to match the subduction zones as in the longitudinal dimension. Transitions to subcritical of the G^2 profiles in this dimension appear to coincide with the lateral intrusion expansion that is marked by a deepening of the pycnocline and baroclinic gradients in the deep layer.

E. HYDRAULIC CONTROL MECHANISMS

The basin geometries examined allow for control of the intrusion front by either depth or width, or both. Symptomatic of the varying influence of expansion versus depth control, PF locations are observed to evolve differently in each model run (recall Figure 6). SWPs in the open basin simulations do not expand to fill the estuary as in the narrow basin cases or field studies conducted in constricted estuaries, allowing lateral expansion of the SWP to be examined here. Length scales from front to toe are an order of magnitude larger in the longitudinal dimension than laterally, complicating direct comparisons. To describe the roles of expansion and depth in controlling PF location and shape, 2D techniques are required.

1. Plunge Section

The critical plunge dimensions, h_p and b_p, can be evaluated using Eq. 2-3 at any location with collocated velocity and density profiles. In a spatial array of such measurements because both h_p and b_p are rearrangements of the same volume flux conservation equation, the plunge point will conform to a line of mutual realization for h_p and b_p, which is referred herein as the “plunge section”. Although difficult to evaluate in the field, this assessment is straightforward using model output.

The shape of the plunge section can be used to characterize whether depth or expansion preferentially acts to release the flow from hydraulic control and allow a front to form. Consider a water parcel transiting supercritically ($F_0^2 > 1$) into a basin. The parcel can “feel” the width and depth of the basin at its present location to determine whether it continues unobstructed or interacts with the ambient estuary water. While both critical values calculated by Eqs. 2-3 exceed the physical dimensions of the basin, the inflow remains supercritical. No fronts will form nor plunges occur until the parcel reaches a location where either critical dimension is achieved. In flat or laterally uniform bathymetry, the entire section at that width achieves both its critical width and depth simultaneously, and the plunge section, connecting all of the mutual realization points, traces the linear cross section. Contrast this expansion released plunge section to one involving a deep central channel. The plunge depth (and mutually the plunge width) now occurs much closer to the control point within the deep channel, but farther into the estuary as the depth decreases away from the center of the channel. A V-shaped plunge section results that is considered depth released. The acuity of the "V" suggests the influence of the depth release relative to the expansion release in allowing the generation of the surface front.

To apply this method to the current analysis, velocities and depths are calculated individually by grid cell. Width varies only in the along stream dimension, which assumes that flows widen linearly vice radially. The plunge section is defined as the contour of $b - b_p = 0$, which coincides with $h - h_p = 0$, which is plotted in Figure 6 as a solid line in a matching color to the corresponding PF. The plunge sections of model runs with a more distant bathymetric break are released purely by expansion (straight lines at x~4500, Figure 6a,b). Moving the bathymetric break closer to the inlet changes the plunge section to reflect depth release of hydraulic control at the front (Figure 6c). The differing PF character in the deeper profile is directly associated with this shift in control release mechanism (compare arrowheads in Figure 6c vs. Figure 6a,b). Compared to the distant slope cases, the deeper profile allows stronger central flows and confines the lateral expansion. The lateral expansion permitted in the flatter bathymetries generates not only wider plumes and plunge fronts, but also less acute shapes of these features.

It is noted that the plunge sections describing the mutual realization of Eqs. 2 and 3 do not match PF locations as in previous studies, which happen to treat the critical plunge dimensions independently. In fact, even the longest front trailing edges do not extend back to the plunge section. The interpretation here is that rather than explicitly predicting the location of the front, calculating the plunge section by this unified method describes a sort of virtual internal control point. Beyond this point, a water parcel is released from the hydraulic control of the inlet, but only plunges when acted upon by other factors such as the slope break (if expansion released) or the SWP interface. The advance of the front is then determined by advection and expansion of hydraulic information envelopes. This virtual internal control may also mark the transition between the supercritical tail of the intrusion and the turbulent lateral dissipation region [*Lowe et al.*, 2002]. If so, the plunge section character may provide clues to whether the SWP will expand laterally (expansion released, Figure 6a,b) or not (depth released, Figure 6c).

2. Froude Angles

The findings of this study suggest that in certain circumstances it may be possible for subduction to occur in the supercritical flow region (early in the flood phase, Figure 7a-d; near the trailing edge of a plunge front, Figure 7e, i) rather than at the critical transition as hydraulic theory dictates. Froude angles are used to describe the transmission of hydraulic information in 2D horizontal flows with fronts oriented obliquely to the principal flow direction [*Garvine*, 1982]. While not an explicit assessment of the front location, *MacDonald and Geyer* [2005] applied this method to explain the shape and control mechanisms of bottom ebb lift-off fronts along the shelf break at the mouth of the Fraser River. Here, this technique is evaluated for adaptation to the prediction of tidal intrusion fronts.

In unidirectional geophysical flows, an alternate interpretation of the Froude balance is a ratio of the ambient flow velocity (u) to a gravitational wave speed (c). In two dimensions, radial expansion of the wave front creates an envelope within which the wave information is contained [*Garvine,* 1982]. Under critical flow conditions (F=1), the wave speed is equal to the flow velocity ($u = c$), so that the wave propagates exactly back to the initial disturbance point as it is carried downstream (Figure 10a). In supercritical flows (Figure 10b), the advection outpaces the wave propagation ($u > c$) and detaches the entire expanding disturbance from its source. The symmetrical information envelope is now bounded by the half-angle φ formed between the direction of the ambient flow and a line emanating from the initial disturbance through a point that is tangent to the wave circle. *Garvine* [1982] defines φ as the Froude Angle

$$\varphi = \sin^{-1}\left(F^{-1}\right). \tag{9}$$

For a supercritical flow at the information envelope, $\alpha=\varphi$ can define an axis rotation such that the flow is broken into components that are parallel and orthogonal to the envelope (Figure 11c). If a front occurs along the envelope (wide gray line, Figure 10c), the flow component orthogonal to the front must be assumed to be in critical balance with the buoyancy in the traditional one dimensional sense

$$F \sin \alpha = 1, \tag{10}$$

in which case we might call it the “critical vector”. The component parallel to the front would then describe the transmission of hydraulic information along the front (the “information vector”).

For the basins in this study, the information being propagated is the basin expansion. The ambient flow will advect that information along the basin shores, which also constrain the outward boundary of the information envelope (Figure 11a). Once the basin attains its maximum width (T3, Figure 11a), continued information expansion will necessarily force the boundary to impinge upon the central, uninformed, supercritical flow from each side, creating the convergence necessary for frontogenesis to occur.

In a two-dimensionally varying flow field, Equation (9) can be used to invert the problem by calculating a local axis rotation α for each velocity measurement location, such that a critical vector is defined in every location whether a front is present or not (thin vectors in Figure 11b). Flows that are less supercritical (larger α) on the informed side of the front and more supercritical (smaller α) on the uninformed side define a field of information vectors that converge upon what can be considered a preferred envelope boundary and front location (wide gray line in Figure 11b). If a streamline is drawn along the information vector convergence, a boundary is defined, the supercritical side of which the flow will not have received information about the expansion. Instead, the information is restricted to the less supercritical (or subcritical) side, contained in the present scenario between the lateral margins of the basin and the information convergence boundary, as depicted in Figure 11a. The interpretation is that a front forming on the downstream (subcritical) side of this boundary is influenced in part by the expansion, but a front forming on the upstream (supercritical) side cannot yet “feel” the influence of the expansion at all, and necessarily must be controlled by some other factor such as depth.

The results of an analysis using this predictive tool are shown in Figure 12, which compares the computed information envelopes to the diagnosed plunge front locations. The axis rotation α is calculated and then applied at each grid point to the depth-averaged velocity vector to obtain critical and information vectors at each location. Streamlines connecting the information vectors are drawn originating from the control point to describe the separation of expansion information from the main supercritical flow (black lines, Figure 12). The central region contains *only* information from within the inlet, and the envelope describes the maximum inward encroachment of the expansion information from the margins of the basin.

The expansion envelope extends in the along-stream dimension from the control point to the transitional F^2 zone (Figure 12). Initially very narrow (Figure 12a), the envelope expands laterally as the flood flows strengthen to help determine the PF width. The T1 plunge (cyan contour) is not aligned with the expansion envelope, but at T2 shows close alignment with the expansion envelope (Figure 12b). PF alignment with the edge of the expansion envelope degrades slightly at T3 (Figure 12c), particularly at the outboard trailing ends of the front.

The plunge front does not align in any sense with the expansion envelope at T1 (Figure 12a), both trailing the leading edge and extending beyond its lateral boundary. The plunge is thus presumed to occur in response to a factor other than the expansion of the basin -- most likely the bathymetric break. Review of PF patterns at individual model times surrounding the T1 step (Figure 12d-f) appears to confirm this hypothesis. The stationary plunge feature at the slope break (x=4500) appears in the first time step (T1-20 minutes, not shown) that the inlet flow turns into the back bay. The PF appears approximately 200 m up estuary from the break in the very next time step (T1-10 minutes, Figure 12d), and reaches alignment with the leading edge of the expansion envelope, assumed to be its dynamic equilibrium position, between 40 and 60 minutes (T1+20 minutes to T1+40 minutes, not shown) following flow reversal.

These findings demonstrate the importance of the slope break on PF formation, and the implied influence of depth helps to explain why the width of the front is limited in the early stages. Information on the slope break travels with the flow just as does expansion information, so information envelopes are recalculated from this feature (the "slope break envelope", red lines in Figure 12) to assess its importance. Since the advancing depth-controlled plunge front is mostly unaware of the expansion at T1 (Figure 12a), the slope break envelope appears to limit the lateral extent. The PF aligns with both expansion and slope break envelopes at T2, but by T3 the PF is insufficiently correlated at its trailing edges with either the slope break or expansion envelope (Figure 12c) to determine which is controlling PF location. Information flow lines are again recalculated, this time from the plunge section where the critical plunge depth h_p and width b_p are mutually realized (Figure 12a-c). Information of attaining the critical plunge section (the "plunge envelope", gray streamlines) appears to complete the PF alignment at the trailing edges (Figure 12c). The implication in this case is that within the expansion envelope, fronts can be additionally influenced by information flowing from the plunge section.

The resulting pattern is a central slope break envelope that contains slope break information, the region outside the expansion envelope that contains only expansion information, and the area in between that contains neither. Encompassing it all is the plunge envelope containing information that the critical dimensions have been attained. In every case the plunge front follows the plunge envelope best, but consideration of all of the envelopes allows interpretation of the control mechanism and expected character of the front as well. The gravity current flowing down the bathymetric slope at the break induces a surface plunge. This is not coincident with the primary density gradient, and so may not be technically considered a front, but nonetheless likely provides the frontogenesis mechanism. The hydraulic information vectors push the plunge front forward until it reaches the leading edge of the slope break envelope. Here the PF encounters the density gradients that induce subduction and create a proper tidal intrusion front. This is also the first encounter of the PF with expansion information. The PF begins to laterally expand to reach the expansion envelope. At T2 (Figure 12b, y+/-150 m), the expansion and slope break envelopes overlap in the center, but the PF has also reached the expansion envelope in the lateral segments. This change in control mechanism appears to correspond with the offset in the PF. When the PF extends to the separation between the expansion and plunge envelopes at T3 (Figure 12c, y+/- 300 m), it continues expanding laterally following the plunge envelope, changing character again to be more intermittent. All the while, the central portion has continued to align best with the slope break envelope, accentuating the offset created by the ever-widening separation among information envelopes. This seems to indicate that the plunge front location in the lateral segments, controlled primarily by expansion, is advancing outward, particularly near the trailing edges, while the central segment is advancing forward because depth is the dominant contribution to its control. This transition of control mechanisms would also help to explain the changes observed between and across the discrete lobes at T3 in the shallow slope case (recall Figure 6b, cyan arrowheads), since the lateral expansion is likely more forceful in the shallower water near the inlet. In the case of the close slope basin (Figure 6c), the lateral expansion is limited by the long time it takes the front to reach dynamic equilibrium at the leading edge of the slope break envelope, as well as by the narrowness of the expansion envelope once it does reach that information envelope (not shown).

F. CONCLUSIONS

The idealized hydrodynamic model domains studied here are designed to examine tidal intrusion fronts in a broad, shallow estuary that would be considered well- to partially-mixed. The flow and density structures are examined to evaluate the forcing relationships associated with the observed features. Force balances between inertia and buoyancy (Froude numbers) remain the most straightforward means of evaluating tidal intrusion fronts and reveal insight into frontogenesis mechanisms of tidal intrusion fronts.

Delft3D-FLOW resolves tidal intrusion fronts and is appropriately sensitive to variations, resulting in tidal straining or location shifts when ΔS varies. Resolution is sufficient to show finer details of the intrusion as well, such as dissipation features behind the leading edge of the intrusion. Force balance irregularities along the lateral margins of the SWP (e.g., Figure 7e,h) hint at elevated flow velocities in the model that would be characteristic of these regions [*Lowe et al.,* 2002].

Structural evolution indicates that downslope gravity currents form almost instantaneously near the centerline, generating surface subduction at the supercritical slope break. Lateral expansion along the expansion envelope begins once the SZ reaches equilibrium near the SWP leading edge. The PF slows its advance, but expands laterally as the subsurface gravity current advance accelerates, likely facilitated by the residual deep stratification. The SZ may be decoupled from the gravity current, requiring individual attention in the future to fully understand. The toe of the intrusion is consistent with the behavior of the intrusion "head" from previous laboratory experiments [*Lowe et al.,* 2002; *Gristenko and Chubarenko,* 2010]. The intrusion toes are active up-estuary of an active SZ and PF. Density structures and surface gradients are the most definitive PF locator, as expected for a hydrodynamic model study, but F^2 and F_Δ^2 are also good diagnostics. Contrary to *Thain et al.* [2004], however, F_Δ^2 does not show the best PF alignment. Rather, F^2 lined up most reliably, has the added utility of describing the SZ's subsurface extent, and may even be able to distinguish actively advancing regions of the front. Composite Froude number G^2 shows limited use in determining front location. Structure, flow, and force balance relationships are observed laterally in an equivalent sense to the longitudinal dimension, but at much smaller length scales, necessitating the employment of two-dimensional techniques to evaluate frontogenesis and hydraulic control mechanisms.

Calculation of critical plunge width b_p and depth h_p as a coupled system rather than independently allows for evaluation of whether the intrusion front is released from hydraulic control by expansion or depth, or a combination of the two. For the cases in this study, a clear distinction is evident between the fronts in depth and expansion released basins (Figure 6, compare a/b with c). Shallow, expansion controlled bathymetries generate broad, crescent shaped fronts that quickly reach dynamic equilibrium and then expand laterally. Depth controlled basins produce V-shaped fronts that advance more rapidly but take longer to attain dynamic equilibrium, and thus do not expand laterally. SWP expansion in a narrow basin quickly reaches the sides and limits evaluation to the longitudinal dimension only.

Froude angle rotations evaluate how expansion and depth information is transmitted to and influences the plunge front. Plunge envelopes appear to be the principal information pathways determining the dynamic equilibrium position of the front (Figure 12). The slope break envelope contains the frontogenesis mechanism, but constrains the lateral extent of the front until it reaches the expansion envelope, which allows it to expand laterally while the slope break envelope continues to influence the shape of the central, partially depth controlled PF segments. The leading edge of the slope break envelope defines the portion of the front that advances forward, but where the PF extends along the expansion envelope, it becomes informed by expansion, and advancement will have a lateral component. In a basin where control is released by depth, the front takes longer to reach the dynamic equilibrium of the plunge envelope, limiting the opportunity for lateral expansion, which is also limited by the narrowness of the expansion envelope. This newly understood composite control mechanism could have implications on the impact assessments for anthropogenic "improvements" to an estuary.

Although the general differences between expansion and depth control are shown in this analysis, the exact details are not explicitly enumerated in this study. The precise nature of the bathymetric sensitivity should be examined in greater detail if these techniques are to be employed as a planning tool. Quantitative scales and relationships are left out of this analysis in favor of general comparisons due to the extreme generality of the model domain and known limitations of the model physics.

The two-dimensional hydraulic control evaluation techniques used in this study demonstrate how changes in the bathymetry can change the character of a convergence front by altering its control mechanism. Consider an estuary that has not been dredged for some time, allowing sediment to build up within a central channel. Dredging a channel through the shoal and/or basin could quickly change the hydraulic control and/or release mechanism, reorienting and relocating the intrusion fronts significantly, along with sediment, larval, and pathogen pathways, navigational hazard zones, and other secondary effects [*Ralston, et al.,* 2012]. The techniques and interpretations developed by this study may serve as a guide for engineers and scientists to apply to actual bathymetry and physical forcing in developing an assessment tool to understand the impacts of artificial "improvements" such as dredging or natural processes such as sea level rise to the dynamic equilibrium of estuarine systems.

THIS PAGE INTENTIONALLY LEFT BLANK

III. STRATIFIED CONFLUENCE FRONTS IN A SHALLOW COASTAL PLAIN ESTUARY

A. INTRODUCTION

The distribution and behavior of estuarine fronts have significant implications for circulation pathways, residence times, and fates of biota, pathogens or contaminants released into an estuary. The spatial and temporal distribution of sediment transport within an estuary is also influenced to a great degree by front occurrence. Assessments of the circulation patterns and mixing processes occurring within an estuary are often possible from increasingly available remotely sensed front data [*Giddings et al.*, 2012]. Modern hydrodynamic models are also capable of resolving both fronts and mixing mechanisms (Weltmer et al., manuscript in preparation, 2013). However, unsupported assumptions based on estuarine classification, such as expected front or mixing type, if favored too strongly, can result in erroneous conclusions. It is therefore imperative to fully understand the range of processes potentially at play within a given estuary. Correct prediction allows for the development of effective strategies to reduce, mitigate, or adapt to the significant impacts these processes can have on public health, navigation safety, and economic development.

The general assumption is that stratified fronts do not occur in estuaries classified overall as well-mixed. As the name implies, this class of estuaries are generally assumed to be dominated by vigorous vertical mixing. Axial convergence fronts are therefore the most common type of front, and tidal straining is the most likely mechanism for stratification. Tidal current shears between shoals and a central channel in a long estuary result in transverse circulation cells that generate axial convergence fronts [*Li*, 2002]. They are strengthened when coupled with a longitudinal salinity gradient at the break [*Nunes and Simpson*, 1985; *Valle-Levinson et al*., 2003]. The convergence here is a surface expression of the very mechanism that mixes away stratification [*Nunes and Simpson,* 1985; *Li*, 2002; *Valle-Levinson et al.,* 2003]. Tidal straining commonly occurs in shallow, friction-dominated estuaries. Though not associated with fronts, tidal straining produces stratification over broad areas by distorting the horizontal density gradients, even in well- or partially-mixed estuaries [*Simpson et al.,* 1990]. While vertical mixing is linked directly to the classification of well-mixed estuaries, stratified intrusion fronts often *suppress* vertical mixing [*O'Donnell et al.,* 2008; *Giddings et al.,* 2012], making these features more common in partially-mixed or salt wedge estuaries. Tidal intrusion fronts appear where dense flood tidal flow converges with buoyant outflow in the lee of a shoal or constriction that imposes hydraulic control on the inflows. [*Famer and Armi*, 1986; *Largier*, 1992]. The induced stratification that defines intrusion fronts forms the basis of the generally accepted view that they do not occur in well-mixed estuaries. Field observations of tidal intrusion fronts in a well-mixed estuary are thus neither discussed nor documented anywhere in the literature.

The hypothesis posed herein is that densimetric intrusions can, and do, appear where bathymetric controls, segregated mixing, and flow convergence occur synchronously. The potential for tidal intrusion fronts in a well-mixed estuary has been suggested by model simulations (Weltmer et al., manuscript in preparation, 2013). This paper follows up on this idealization by presenting field observations of a bathymetrically-induced, stratified intrusion front in a well-mixed, coastal plain estuary. After describing the instrumentation and sampling scheme in "Methods", the observed intrusion front is described in "Results". Front measurements are consistent with tidal intrusion fronts in form, but direct comparisons are difficult owing to the unusual confluence of flows at the front created by complicated morphology. This is contrary to the accepted view of tidal intrusion fronts that requires flow *convergence* in a confined waterway to decrease the composite control state at the front. In fact, the confluence observed here creates supercritical flow on both sides of the front, also contrary to the supercritical-to-subcritical transition proposed by hydraulic theory. To address these inconsistencies, the "Discussion" section explores field validation of a Froude angle technique to identify a dynamically preferred front location and orientation within distributed flow fields. This will allow for an axis rotation that results in a front-normal Froude profile that is consistent with hydraulic theory. Context is broadened by using a pre-validated hydrodynamic model to propose a mechanism that produces mid-density water inside a segregated side bay and unites it with dense ocean water just in the lee of the shoal that acts as a hydraulic control feature. In the

"Conclusion" the importance of front classification is reviewed, as well as the impact and utility of correct identification and prediction. Potential exists for the techniques used herein to serve as the foundation of a toolkit to enable local environmental planners to accurately assess the hydrodynamic and geomorphological impacts from human improvements such as dredging, extreme events like a hurricane surge, or changes to external forcing such as a heavy rainfall event.

B. METHODS

Field measurements were collected 1-21 May, 2012, in the New River Estuary (NRE) during the River Mouth and Inlet Dynamics (RIVET) project. The experimental goals were to study the wave, current, and exchange processes associated with an estuary inlet. The data collected for this study form the basis for a semi-quantitative description and classification of a front that forms regularly inside the estuary. Other data collected for related studies provide additional context that are used to support these conclusions. A high-resolution Delft3D-FLOW model domain of NRE is used to *qualitatively* confirm the conclusions drawn from measurements and explains the circulation patterns that allow the front to form.

1. Study Site

The New River Estuary (Figure 13a), North Carolina, is a shallow, tidally dominated coastal plain estuary [*Dame et al.*, 2000] connecting the small (~80km), weak New River to the Atlantic Ocean via the unusually long (~3km) and narrow (200-300m wide) New River Inlet (Nautical Chart 11542 "New River", 18th Ed., Corrected through June 2013, available at Office of Coast Survey, www.charts.noaa.gov). The estuary is bounded on most sides by tidal creeks and marshes [*Koroknay*, 2012], and is dynamically connected to adjacent inlets to the north (Browns Inlet, 12 km away) and south (New Topsail Inlet, 36 km distant) by the Atlantic Intracoastal Waterway (ICW) (Figure 14). The New River Inlet and ICW have been built and maintained for decades by side-cast dredging [*Ryscavage*, 2010], which has effectively extended the primary tidal channel into the back bay and created artificial islands (Figure 14, dashed oval) that separate the primary tidal channel from Traps Bay to the north and the unnamed side bay to the south.

Surveyed water depths are 6-8 m in the New River Inlet, and 4-5 m in the extended portion of the tidal channel. However, with the exception of the primary navigation channel though the back bay (~3.5 m), depths do not exceed 2m anywhere else in the estuary (Chart 11542, 2013).

Tidal forcing is dominated (84%) by the M2 lunar tidal constituent, with the remaining primary astronomical constituents (K1 S2, O1, and MSF) combining to account for 93% of the total variance (MacMahan et al., Fortnightly tides and subtidal motions in a choked inlet, submitted to *Estuarine, Coastal, and Shelf Science (ECSS),* 2013). Offshore amplitudes range from 1.2 m (neap, 14 May) to 2.2 m (spring, 6-7 May), with an ebb-dominant diurnal inequality (lower low water precedes higher high water). Owing to the shallow bathymetry and strong tidal currents (> 0.5 m/s) of the NRE, bottom friction is a dominant response term and also shown to be a critical factor in correctly modeling the tidal variability from offshore to the bridge (MacMahan et al., submitted to *ECSS*, 2013). The result is vertically mixed profiles throughout the inlet and back bay [*Sheets*, 2013], with few exceptions, and a general circulation-based classification of "well-mixed" [per *Hansen and Rattray*, 1966]. Tidal amplitude reductions and phase lags vary with frequency, but are significant from offshore to the head of the artificial flood delta (87% reduction and 2 hour phase lag for the diurnal frequency band), additionally resulting in a morphodynamic classification as tidally "choked" [*Kjerfve*, 1986]. Though both of these classifications result in the assumption of weak vertical stratification, *Kjerfve* [1986] and *Hansen and Rattray* [1966] are both quick to acknowledge the weaknesses of any generalized classification procedure – comparable magnitudes among the forcing terms and significant spatiotemporal variability make it difficult to separate the dynamic processes of tides, wind, and density currents.

Wind forcing during May (available at State Climate Office of North Carolina, www.nc-climate.ncsu.edu) prevails at 10-15 kts from the SSW under the building Bermuda high to the SE, but can be highly variable during the spring transition season. Low pressure systems pass the area ~weekly during May, typically well to the north. In unusual cases a powerful low may pass very close, bringing 30-40+ knot winds from the

NNW to the area. Diurnal sea breezes are common, particularly on days that are less energetic overall. Front data were collected during days of minimal wind forcing (S 5-10kts) and no rainfall in the days preceding the observations. This minimizes the influence of wind-driven circulation as well as river discharge, leaving the system to be driven almost entirely by the tides.

As an estuary with a well-mixed circulation type, oceanic water is expected to reach well into the back bay during flood tide, mixing with the ambient estuary water at the advancing gradient through the action of bottom friction. Gradients are weakened though this vertical mixing, and fronts that form are typically of the axial convergence variety—no stratification is anticipated to develop. The ebb outflow through the inlet is expected to be dominantly composed of that same slightly modified ocean water, until unmodified estuarine water reaches the inlet, perhaps at the very end of the ebb. Stratification may develop as a result of tidal straining, but widespread rather than localized at a convergence. The influence of the ICW on the NRE tidal exchange is expected, but details are unknown without field measurements. One of the fronts that regularly forms during the tidal flood in the NRE, however, becomes stratified, which is highly unusual for a well-mixed estuary. The focused field campaign described in the next section explored the roles played in generating this unique feature by tidal dominance, shallow, complicated bathymetry, dynamic connections to adjacent inlets through the ICW, and artificial fortification of the inlet channel and flood delta.

2. Instrumentation

The oceanographic data presented here were collected during the RIVET experiment (Table 2). Bathymetry data are a combination of historical data (GEODAS, www.ngdc.noaa.gov/mgg/geodas/) and surveys during the experiment (USACE and J. McNinch, unpublished data, 2012). A composite bathymetry map of the back bay (Figure 14) labels geographic features and shows moored instrument locations (✚). The data collection sites near the location of the front are shown in Figure 15. Detrended offshore tidal elevations measured in approximately 9 m water depth outside the ebb tidal delta are shown in Figure 16, along with sampling times discussed in this paper.

The coordinate system employed is a common reference to all RIVET investigations, whereby the true coordinate axes (depicted by North arrow in Figure 13a) are rotated counter-clockwise by 58 degrees to align the x axis perpendicular and the y axis parallel to the local shoreline (axes depicted in Figure 13a). Coordinates are presented in meters from the origin, which is centered in the New River Inlet entrance (shown as crosshairs in Figure 13a).

a. Moored Instrumentation

Stationary data were collected from more than 40 temporary mooring sites throughout the inlet, back bay, and ICW both north and south of New River. This was accomplished through the repeated deployment of six small catamarans ("mini-cats") that were anchored to the seabed. Each mini-cat was equipped with a robust suite of battery powered instruments. A RBR pressure sensor sampling at 1 Hz was attached to the mini-cat anchors to measure sea-surface elevation. A RBR conductivity, temperature and depth sensor (CTD) fastened to the anchor line ~0.5 m below the surface measured conductivity and temperature at 1 Hz. A downward-oriented Nortek Aquadopp Acoustic Doppler Current Profiler (ADCP) transmitting at 2 MHz was attached to the underside of each catamaran hull ~25 cm below the water surface. Velocities were recorded in 50 cm vertical bins starting at ~80 cm below the water surface and averaged over 10 minutes, or 1 minute for deployments targeted at front collection. Mini-cat data presented here were collected during the 8-9 May deployment, which spanned 3 flood tides, and a shorter (~5 hours), targeted 13 May deployment (locations shown in Figure 15). Measurements discussed in this paper are summarized by collection day in Table 2.

b. Boat-Mounted Transecting Instrumentation

For surface transect measurements through the front, an RBR CTD logging at 1 Hz was mounted on the hull of a 17 ft vessel ~50 cm below the water surface. GPS data were logged concurrently at 1 Hz using an Ashtech ZXtreme dual channel receiver. Subsurface profiles were collected with a RBR CTD logging at 6 Hz and mounted to an stainless steel cage that was hand-lowered from the vessel performing the transects. The vessel traveled across the front along the line of mini-cats at speeds less than ~1.5 m/s, collecting a direct surface transect in one direction (inward) and stopping every 10-20 meters for a subsurface profile in the other (outward).

CTD surveys were conducted in consonance with the 8-9 May and 13 May mini-cat deployments (black and blue heavy lines in Figures 14 & 15; Table 2). On 9 May, full profiles were collected along a cross-front line that included the mini-cats at approximately 15-minute intervals for an hour and a half following the peak flood. The 13 May survey collected profiles in a series of cross-front transects that included the line of mini-cats, but extended from the origin of the front near the spoils island to the first major bay constriction, x~5000 m (colored dots in Figure 17). The survey was performed three times in approximately 1-hour intervals starting 1 hour before peak flood. Profiles aligned with the mini-cats are used for the comprehensive analysis that follows, while transects away from the mini-cat line are used only for qualitative comparison of the subsurface features along the front.

c. Autonomous Underwater Vehicle

The survey on 9 May included deployment of a YSI EcoMapper Unmanned Underwater Vehicle (UUV). The UUV surveyed both lateral margins of the channel near the flood front measurement site (thin colored line, Figure 17). This survey was performed at the surface only and collected velocity estimates through the water column from a downward-looking ADCP, surveyed the bathymetry, and measured surface water quality, including temperature, salinity, and chlorophyll and turbidity, from a water quality module housed in the nose of the vehicle. Water quality measurements are used to verify the location of the front (Figure 17), and bathymetry measurements supplement the historical survey data. Velocity data collected by the UUV were suspect and are not included in this analysis.

d. Surface Drifters

The 13 May small boat survey data includes 45 surface drifter tracks, deployed in 5 cross-front lines of 9 drifters each. Each surface drifter is constructed as a 50 cm diameter disk of sealed 4 cm diameter PVC pipe. Although the cross section of these drifters is low (>~10 cm), windage was further reduced and coupling to the surface flow ensured by fastening a 30 cm long drogue of 30 cm diameter PVC to the underside of the disk that hung down to 50cm below the surface. Strapped to the spokes at the center of the disk is a waterproof OtterBox containing a DeLorme BlueLogger single channel GPS receiver recording position at 5-second intervals and a supplemental power supply for increased endurance. These simple but durable drifters were the only source of near-surface flow measurements.

C. RESULTS

First indications of unusual front activity in NRE came during the inspection of publicly available imagery. Aerial photographs taken during high tide show ocean water flooding though the inlet into the dredged channel of NRE (Figure 13b, from Google Earth, July 2006). The boundary between the clear blue ocean water and the darker, more turbid estuary water is very clear in this image. A visible foam line that indicates a surface convergence front marks much of the boundary's leading edge. The northern leading edge of the boundary is unusually distinct for a well-mixed estuary, and comes together at the center of the estuary in a "V" shape. The sharp, "V"-shaped surface convergence signature is the distinct signature of a tidal intrusion front. Images from earlier in the same year revealed similar features (Figure 13c) at an upstream location, indicating that occurrence of these fronts is not unique, which is the basis of the hypothesis that it is possible to generate tidal intrusion fronts in a well-mixed estuary.

A UUV reconnaissance mission was run on May 8 to determine whether the front actually occurred in any of the locations suggested by the imagery. The surface convergence was very apparent, and was traced by small boat and recorded with GPS. The density anomalies measured during the UUV mission are shown as the thin colored line in Figure 17, and the front location using GPS is shown as the black dashed line. A strong density gradient (~1.5 – 2 kg/m^3) across the front trace can be seen as a transition from warm (dense) to cool (buoyant) colors. Boat-mounted CTD traces (wide colored line, x~4500m, Figure 17) reinforce the discontinuity and its alignment with the visible surface front. Surface densities from a field of CTD casts on May 13 confirm both the strength and location of the front. The UUV density measurements show a weaker gradient on the south side of the channel, but no foam line was visible that joined to form a V. From these measurements and repeated visual reports of the front on a number of days during the experiment, it is concluded that the front forms nearly every tidal cycle during flood tide from the landward side of the flood delta into the center of the channel (Figures 15 & 17, dashed trace A-B). The density discontinuity across the front is consistent at 1.5 – 2 kg/m^3. There is no apparent influence from tidal range or spring/neap cycles (Figure 16). To determine whether this could be a tidal intrusion front, the subsurface structure of the front is considered next.

1. Subsurface Structure

Cross-sections of density anomaly and cross-stream velocity vectors at two times after peak flood on 9 May are presented in Figure 18, looking seaward. The near-surface CTD measurements (color scaled profile lines) show the distinct density discontinuity at the front (y~480 m) 45 minutes after peak flood (Figure 18a); the density difference and local gradient across the front near the surface reached up to $d\rho \sim 1.0$ kg/m^3 and $d\rho/dy \sim 0.2$ kg/m^4, respectively. The profile clearly shows that the dense water from the main channel (to the right of figures) underlies the mid-density water to the north of the channel at this location. The region of vertical stratification occurs in the lee of the sill, which is located at y~460 meters. ADCP measurements depicted as arrows show that the main channel flow is barotropic over the sill, as indicated by the logarithmic velocity profile (e.g. M082, directly on the shoal at y~460 m). Enhanced deep flow of the dense water downslope of the sill is observed in the M083 (y~475 m) profiles for both times is suggestive of the subsurface advance of a gravity current under the buoyant layer. Half an hour later, 75 minutes after peak flood (Figure 18b), the total density difference over the front is similar, but is now broken into two discontinuities, one at the surface front (y~480 m) and a second at y~520 with a 40 meter wide mixing zone in between. Velocities do not appear to have decreased to cause this mixing, although the dense ocean water does appear to have advanced somewhat farther under the mid-density water, enhancing the vertical stratification (y~520 meters). While performing CTD cast transects, it was noted that the main surface front was readily visible as a strong foam line coincident with the surface salinity discontinuity. However, foam was also visible on the stratified side of the front that appeared to be bound between the main surface convergence and a secondary foam line. This secondary foam line was later determined to correspond with the location of the toe of the gravity current at y~550 m. This intriguing observational finding suggests that surface flow is convergent within the entire extent of the densimetric intrusion, but non-convergent or divergent outside of this region.

The appearance of such stratification – aligned with the surface convergence, in the lee of a sill that could be acting as a control feature, and persistent through the flood tide – fits well with the conceptual model of tidal intrusion fronts. The transition from friction-dominated velocity profiles over the sill to enhanced bottom velocities underneath the stratification is characteristic of the velocity transition for a densimetric intrusion [*Gristenko and Chubarenko*, 2010].

2. Surface Confluence

To assess the degree to which surface convergence influences the surface fronts, surface drifters were deployed on May 13 in 5 groups of 9 each. Drifter traces, colored by deployment group, are shown in Figure 19a. Red and orange traces were deployed on the main channel side of the front; blue and cyan traces were deployed within the foam region corresponding to the densimetric intrusion; yellow traces were deployed outside of the secondary foam line. Drifter release locations are depicted in all cases by green dots. The warm and cool colored traces depict the distinct surface flow convergence coincident with the GPS trace. The yellow traces released outside of the main front region are not observed to converge with the others, instead travelling parallel to the cyan release group until about x~5000. Landward of this location, the yellow traces diverge from the front, while the drifters that had already converged at the front remain tightly clustered along the front. This result suggests the presence of a surface return flow to complete a cross-front circulation cell contained within the stratified front region.

More interesting, there is a lack of evidence for a seaward outflow of buoyant estuarine water. In the tidal intrusion front conceptual model, buoyant outflow is viewed as a necessary element to generate surface convergence and sustain the density gradient between water masses. Here, apart from the expansion of the flow landward of x=5000m, no eddies, recirculation, or opposing flow is evident in the drifter data. The flow is *confluent* rather than convergent, travelling uniformly landward. The surface velocity structure (Figure 19b) supports transverse-only convergence as the longitudinal surface velocities are enhanced in the confluence region. These observations suggest that the mid-density water on the lateral side of the front originates from Traps Bay, seaward of the front, rather than landward of the front. Not only does this contradict the conceptual model of tidal intrusion fronts, it also indicates that the mid-density water source is Traps Bay, seaward of the front, rather than estuarine water from landward. To confirm this front as a tidal intrusion front, force balances must be examined and a mechanism must be proposed that would describe Traps Bay as reliable source of mid-density water.

3. Temporal Evolution

Time series of density from May 13 mini-cat data (Figure 20) describe the temporal progression of the front. M083 (from 8-9 May deployment) is located directly on the surface front (see Figure 18). The front advances quickly across the mini-cat positions until passing M132, approximately 1 hour into the flood (t~2 hours, Figure 20), when its advance across the mooring positions is stalled. The density increase later reaches M133 and M134 on the lee side of the front (t~2.5 hours, green and cyan), but is less significant. The surface front stabilized its position near M083 and the water mass characteristics across the front remain segregated. Mini-cat positions over the shoal (M131, M132) increased their density to match that of the incoming ocean water (not shown), while those farther off-center remain at a lower density. Fluctuations between water masses of ~1.5 kg/m^3 are observed throughout this time at M083, directly on the front, and less so in M133, located over the stratification zone. Oscillations in the front line were visually observed in all cases. Velocities did not show corresponding fluctuations. It is surmised that these oscillations represent episodic horizontal mixing across the front. It is unclear from the data whether these oscillations propagate through the full depth of the front interface or have a matching vertical component in the subsurface stratification.

Colored cross-sections of linearly interpolated CTD casts are shown in Figure 21 and overlain with cross-stream velocity vectors measured by the mini-cat ADCPs (black) and surface drifters (red). The water on both sides of the front becomes progressively denser through the flood tide (compare Figure 21 a-b-c). Drifter velocities (red vectors, Figure 21a) converge at the surface front location, generating the lateral circulation cell in the stratification zone that is suggested by the foam region at the surface and helps to create and/or sustain the surface convergence at the front.

The form of the front – the depth of the pycnocline, the position of the surface front, and width of the stratification zone – remains remarkably constant through the observation periods, though a slight regression (~15 meters) toward the sill can be observed over time in both Figures 18 and 21. The drifters were observed to converge upon the surface front in each release. Although this is consistent as a whole, examination of each set of drifter releases individually also reveals slight regression in the convergence line over time (Figure 19). M083 density oscillation continues but drops in density (Figure 20, t~4.5 hours) to oscillate across the opposite side of the front (green and cyan), also an indication of a retreat in the front location.

D. DISCUSSION

Overall, this convergence front is a repetitive feature that occurs in this estuarine system on most flood tides. Anecdotally, visible evidence of the front was significantly displaced from this location on days of more substantial wind forcing. The front persists at this location (Figure 15, 17) through the duration of the flood, until just before the flow reverses to ebb. The persistence of the front indicates that salinity differences are maintained through the flood, the reason for which is uncertain given the common landward flow directions on either side of the front. The confluent surface flow at the front suggests that this is an axial convergence front, but examination of subsurface structure and evolution provided the first indications of stratification. The front first appears very soon after flood begins locally and persists through the flood until the next slack. The front results from a confluence of mid-density water from Traps Bay with ocean density water in the main channel as the two flood flows reunite. The front occurs along what now appears in the bathymetry to be a Traps Bay exit channel in the lee of a sill that separates this secondary channel from the main channel through the inlet extension through the dredge spoils (Figure 15, 17, red dashed line). The front stretches from the tip of the spoils island to ~3 km up the back bay and persists for nearly five hours, remaining remarkably stationary throughout the duration of its existence. The location, repetition, and stability of the feature indicate strongly that this front is a tidal intrusion front.

1. Front Type

To confirm the frontal structure and evolution described in the previous section as a tidal intrusion front, other mixing and stratification regimes should first be ruled out. Stratification often occurs in shallow, well- to partially-mixed estuaries with moderate freshwater output as a result of tidal straining. Also called strain-induced periodic stratification, or SIPS [*Simpson et al.*, 1990], tidal straining is a tidal mixing process by which the vertical shear of a tidal flow dominated by bottom friction results in differential advection that alternately develops and destroys vertical stratification. During the ebb transport of buoyant water seaward, tight horizontal density gradients will be distorted by the differential advection, which is further enhanced by bed and wind stresses to generate 2-layer stratification over broad areas. The process is reversed during the flood, eliminating the stratification. In the current study, however, the observed front develops and maintains its stratification during the *flood* tide, and ebb flows mix it away. Furthermore, because tidal straining occurs over broad areas, it is not a process that is conducive to the formation of surface convergence fronts as are observed here.

The most common type of bathymetrically controlled convergence front observed in well-mixed estuaries is the axial convergence front [*Nunes and Simpson*, 1985], generated by induced transverse circulation that also serves to vertically mix the water column. These features are created during flood tides as a result of tidal velocity shear between the central channel and the marginal shoals. The tidal wave propagates more quickly in the channel, and the shear at the bathymetry break induces a lateral surface motion toward deeper water, compensated at depth by lateral motions toward the shoals

[*Nunes and Simpson,* 1985; *Valle-Levinson et al.,* 2003]. This induces characteristic dual opposing lateral circulation cells on either side of the central channel that generate the surface convergence front. Density fronts along the bathymetry break on either side of the seawater intrusion can enhance the overall effect, although the vertical mixing inherent in the generation mechanism of these fronts keeps these fronts unstratified. The circulation observed in the NRE, in addition to being stratified, shows only a single surface convergent circulation cell in the stratified region (Figure 21), with barotropic upstream flow in the central channel. Although roughly axial in orientation, the offset location of the observed front from the central channel and the absence of transverse circulation on the upstream side of the surface front are inconsistent with axial convergence fronts in other well-mixed estuaries [*Nunes and Simpson*, 1985; *Li*, 2002]. It is therefore concluded that the front is not an axial convergence front, and that tidal straining is not generating the stratification that is observed in this region of the NRE.

The stratification features observed here most resemble those of tidal intrusion fronts, which are atypical of well-mixed estuaries because the stratification of these fronts suppresses vertical mixing. The stabilized location of the surface front in the lee of a shoal (Figure 17) and persistent stratification during flood tides (Figure 21) are consistent with the surface subduction and densimetric gravity intrusion of a tidal intrusion front [*Largier*, 1992]. Further evidence for this hypothesis is the slightly weakened gradient behind the head of the intrusion (Figure 18b), a feature observed in laboratory simulations of densimetric gravity intrusions [*Lowe et al.*, 2002; *Gritsenko and Chubarenko*, 2010]. The lateral circulation in the stratified region and barotropic seawater inflow (Figure 21) also compare favorably to the across-front flow of tidal intrusion fronts [Weltmer et al., manuscript in preparation, 2013]. However, there are some important inconsistencies with the idealized intrusion front model. A typical intrusion front spans the full width of an estuary or primary flow, but the observed front here is oriented obliquely, and only appears on one side of the main tidal flow. Additionally, the longitudinal flow is unidirectional across the front, while opposing longitudinal flow generates convergence in a traditional intrusion front.

2. Densimetric Froude Number

A distinguishing characteristic of tidal intrusion, or any stratified front, is the hydraulic control transition across the surface front. Evaluation of hydraulic control state is performed in one-dimensional flow with Froude parameters, which compare fluid velocities to vertical density gradients in a non-dimensional scale analysis of inertial vs. buoyancy forcing. The basic hydraulic control state of a fluid at any given location and time is described by its densimetric Froude number,

$$F^2 = \frac{|u_d|^2}{g'h} \tag{11}$$

where u_d is depth-averaged horizontal flow speed, h is the depth of the water column, and $g' = g\frac{\Delta\rho}{\rho_0}$ is reduced gravity. The transition from supercritical ($F^2>1$) to subcritical ($F^2<1$) is often abrupt and associated with a hydraulic jump feature. In a baroclinic system, the hydraulic jump occurs as a surface convergence front, as observed here. More importantly for tidal intrusion fronts, the subcritical fluid up-estuary of the surface front becomes stratified to some degree, suppressing vertical mixing between layers and allowing distinct, often opposing flow patterns to emerge. These opposing flows decrease the depth-averaged flow to permit buoyancy forcing to overcome the inertia of the dense inflow.

Froude numbers are calculated from the mini-cat, surface drifter, and CTD cast data collected on 13 May (Figure 21d). This date was selected because the mini-cat locations spanned the width of the frontal zone and because the available drifter data allows a more meaningful analysis. Depth-averaged velocities were calculated from the ADCP data of each mini-cat, but since this data does not include the top 75cm of the water column, the drifter data was added to obtain a more complete depth average. This was done by assuming that the drifter body with a 50cm deep drogue were sufficiently coupled to the near-surface mean flow for its motion to be representative, which then could be added as an appropriately weighted bin for depth average calculations. Because drifters measure surface velocities over both space and time rather than continuously at a single location, drifter velocities were measured as a spatial average of drifter velocities within 10m of each mini-cat location.

The Froude numbers calculated using this depth-averaging method are shown in Figure 21d as a solid black line. The red dashed line marks the critical F=1 point for reference. Froude numbers for each location and each time were supercritical with the single exception of M133 an hour after peak flood (not shown). This is counter to the expectation of a transition from supercritical in the dense water mass (M131, M132, Figure 21) to subcritical in the stratified region (M133, M134) [*Largier*, 1992]. Open basins or two-dimensional flow with obliquely oriented fronts are not necessarily exempt from this general rule [*MacDonald and Geyer*, 2005; Weltmer et al., manuscript in preparation, 2013]. The noted inconsistency with the tidal intrusion front conceptual model is related to the unusual confluent (vice convergent) nature of the flow interaction at the obliquely oriented front. Dominant tidal flows likely overpower weak lateral circulation patterns that emerge, inhibiting the depth-averaged velocity decreases that would otherwise develop in the stratified region and cause Froude numbers to fall below critical. To evaluate this hypothesis, coordinate rotation techniques are required.

3. Coordinate Rotation

To simplify the dynamics, and owing to the dominant principal components of the tidal flows that typically converge to form tidal intrusion fronts, Froude balances are derived in a single horizontal dimension. In this setting, however, the observed front was not oriented orthogonally to the principal flow direction, nor did it span the full width of the basin. Rather, it was significantly oblique to the primary flood tidal flow (~70 degrees from orthogonal), and only present on the north side. Principal component analysis to determine a dominant tidal flow orientation was ineffective due to the complicated bathymetry and confluent flows. As a result, the total velocity vectors were used in the initial Froude analysis presented above. Situations like this call for a technique to determine a preferred front orientation, to which parallel and orthogonal forcing terms can be oriented. Calculation of a Froude angle, analogous to the Mach angle, has in recent years been adapted from the study of surface plume fronts [*Garvine*, 1982] to predict salt wedge ebb lift-off fronts [*MacDonald and Geyer*, 2005] and tidal intrusion fronts [Weltmer et al., manuscript in preparation, 2013].

A Froude angle (φ) essentially defines an axis rotation that divides the total vector of a supercritical flow into cross- and along-front components [Weltmer et al., manuscript in preparation, 2013]. For a velocity measurement located directly along a front, the component orthogonal to the front (and flow) should by definition result in a Critical balance (F=1), defining the surface front as a hydraulic jump, and is termed the "Critical Vector". The residual, along-front (parallel) flow component at that point will describe the translation of hydraulic information exactly along (but not across) the front (the "Information Vector").

In a field of supercritical velocity measurements, or a line of measurements as was collected in this study, not all measurements will lie directly on or near a front [Weltmer et al., manuscript in preparation, 2013]. In this situation, the Froude angle calculation is inverted to compute an angle α at each velocity observation, defining its own axis rotation into a Critical and Information Vector using the form

$$\alpha = \sin^{-1}\left(F^{-1}\right) \tag{12}$$

where F is the depth-averaged Froude number at each measurement location. For a velocity measurement coincident with the front, $\alpha=\varphi$, and the Critical Vector is exactly orthogonal and the Information Vector exactly parallel to the front, describing the balance orientation and information flow, respectively.

Away from the front, α will be greater or less than φ depending on the relative strength of the flow and stratification at each measurement point. If we consider a parallel flow field, and make the assumption that the flows will be more supercritical on the upstream/centerline side of the front, and less supercritical (or subcritical) on the downstream/outboard side of the front, we can deduce that $\alpha>\varphi$ on the upstream side, and $\alpha<\varphi$ on the downstream side. This creates scatter in the Critical Vectors and uncertainty in determining a balance orientation if front observations are not available. However, *Weltmer et al.* [manuscript in preparation, 2013] found that the Information Vectors can be expected to converge toward the front, a finding that can be exploited to determine a data-derived ("preferred") front location and orientation in the absence of front measurements.

Critical and Information vectors for the mini-cat data are plotted as red and blue arrows in Figure 22, along with the tracks of the drifter release (cyan) that best defines the convergence front. The Information Vectors (blue) converge upon mini-cat location M132, which is located almost exactly on the surface front (Figure 21, 22). The M132 Information Vector, in turn, is oriented close to parallel (within 15°) with the front at its closest point to the observation. Were front information not available, the Critical Vector of M132 could be reasonably used to define the axis of balance for the observed front.

Since precise front location data are available in this case, axes are rotated according to the mean orientation of the cyan drifter tracks in Figure 22. Froude numbers are re-calculated using front-oriented components (Figure 21d), which shows that F_l (the along front component, shown in blue) remains supercritical across the front except in the stratification zone, while F_x (across front, shown in red) distinctly transitions from supercritical on the dense (right) side of the front to subcritical on the stratified (left) side, passing critical (F=1) very close to the surface location of the front. The slight retreat of the surface front at each successive hour is also matched by the critical crossing, even using the crude linear interpolation between observations (not shown). This confirms that this is an intrusion-type front, but the fact that finding the appropriate Froude balance transition required the use of Froude angles indicates that an unusual forcing mechanism is at play.

4. Provenance and Frontogenesis

The buoyant water exiting Traps Bay to the north of the front (Figure 20, M133 and M134) remains consistently lower density than the dense ocean water flowing up the primary central channel (M131 and M132), helping to maintain the front through the tidal flood. In fact, despite evidence that the flows through Traps Bay are in the same direction as the primary flood flow, there is no indication that the water in Traps Bay ever assumes the full ocean density. Rather, cluster analysis of temperature, salinity, and CDOM (chromophoric dissolved organic matter) content throughout the estuary defines the NRE in terms of four distinct water masses – ocean, back bay, southern ICW, and a mixed water mass comprised mainly of Traps Bay [*Sheets*, 2013].

To qualitatively assess water mass movements that result in the densimetric intrusion fronts described here, the Delft3D-FLOW shallow water model is employed [*Deltares*, 2010]. Delft3D-FLOW is a fully nonlinear, hydrostatic model designed to simulate shallow water environments from beaches to estuaries to rivers. The curvilinear model grid used here varies from O(100m) resolution offshore to O(10m) in the New River Inlet, near the intersection with the ICW, and in the area surrounding the observed front. The model uses 10 σ-levels in the vertical and includes wetting and drying. The detailed model parameters are taken from a validation effort underway (A. Reniers, unpublished data, 2013) that includes wind and wave forcing, but is simplified here to focus the results on tidal circulation forced by dominant offshore astronomical constituents (calculated by MacMahan, J.H., submitted to *ECSS*, 2013). Though not yet validated for this inlet, Delft3D has successfully simulated fronts and tidal circulations in a wide range of estuarine environments [*Mulligan et al.,* 2008, 2010, 2011]. Here, the model successfully reproduces the front and captures the associated circulations and density variations.

The Delft3D model simulations (simplified and depicted in Figure 23) qualitatively describe the flow patterns and temporal evolution that result in generation and maintenance of the observed intrusion front, and are supported by mini-cat data throughout the NRE (not shown). During ebb tide (not shown), the back bay water mass encompasses much of the region near the front. Lower density water flows from the up-estuary source region out the main channel and into the inlet, but also provides low-density input to Traps Bay, where it is partially sequestered by lower velocities. As the tide transitions to flood (Figure 23a), ocean water flows through the inlet into the extended channel, where some of it splits northward into Traps Bay, providing ocean water input that is mostly retained for mixing. Model results suggest that seaward flow into Traps Bay may continue 20-30 minutes after the channel flows have switched to flood, generating the convergent shears and density gradients (up to 3 kg/m^3 from t=2 – 2.5 hours in Figure 20) more typical of tidal intrusion fronts, after which the confluence and slightly weaker density gradients (~1.5 kg/m^3) are sufficient to sustain it through the flood (Figure 23b,c). After about 2 hours, the influence of adjacent inlets begins to be felt as southward flood currents arrive from the northern section of the ICW and begin to deflect the NRE flow (Figure 23c). This cuts off the input of ocean water to Traps Bay and provides weak input of pre-mixed mid-density water from the northern ICW. Though the dense water is now retained in Traps Bay for mixing, head gradients continue to force already modified mid-density Traps Bay water landward into the front region, where it interfaces with the ocean water of the central channel as described in the previous section. The deflection of the flows as the tide transitions to ebb (Figure 23d), particularly near the front, pushes the oceanic water and surface front to the south before density gradients begin their ebb retreat and the cycle begins again.

E. 5. CONCLUSIONS

A densimetric intrusion front is described in a well-mixed estuary. To facilitate this unique feature in an unexpected setting, artificial dredge spoils islands segregate Traps Bay from the main central channel. This allows production of a persistent mid-density water mass as lower-density estuary water and high density ocean water trade input pulses that get sequestered and mixed in Traps Bay due to lower velocities and long residence times. This mid-density water is then consistently brought into confluence with intruding ocean water during flood tides. Because the convergence occurs in the lee of a shoal that imposes hydraulic control on the dense water flow, the oceanic intrusion is able to subduct beneath the mid-density Traps Bay water as a densimetric intrusion. The front structure is typical of a tidal intrusion front in most aspects, although it is oriented obliquely to the primary ocean flood flow. The confluence is also problematic as it allows minimal shear to develop, keeping the flow supercritical on both sides of the front. This is expected in a well-mixed estuary, but not conducive to formation of an intrusion-type front. The balance orientation of the front is derived using Froude angles to re-calculate front-normal Froude numbers to define the supercritical to subcritical transition expected in the standard view of tidal intrusion fronts.

Stratified intrusion fronts have never before been documented in such a shallow, well-mixed estuary, nor have intrusion-type features been documented in flow patterns other than convergence in near perfect opposition. It is proposed that the bathymetrically-induced confluent subduction observed here is a subset of the broader tidal intrusion front category, or a hybrid front type of axial convergence front, which may help to explain how the front may be able to gradually transition to that type of front farther up-estuary as suggested by the Delft3D model simulation. Key to this type of confluent frontogenesis mechanism, however, is a supporting mechanism that allows a mid-density water mass to form in a side bay or similar lateral location separated from the main flow by shoals or islands. In NRE, the dredge spoils provide the flow separation to allow mid density water to form in Traps Bay, and the shoal deposited near a bend in the central channel provides the hydraulic control near the re-convergence to induce the subduction.

Though the estuary circulation vs. mixing classifications of *Hansen and Rattray* [1966] are understood to potentially vary locally (temporally and spatially), these generalizations are nevertheless used to draw estuary-wide conclusions from remote sensing or model data when in situ data is scarce. The observed generation of an intrusion-type front in what is classified a well-mixed estuary, despite its irregularities, should give pause to coastal scientists and engineers who place great importance on such estuary-wide classifictions. Rather than a transitory vertical mixing zone, the stationary front observed is more likely to inhibit vertical mixing in the stratified portion in favor of the surface subduction and intrusion head regions. This in turn creates well-defined constituent pathways and boundaries, as well as sediment erosion and deposition zones that when repeated every flood tide could lead to unintended or unwanted migration or generation of channels and shoals.

Though further exploration of well-mixed estuaries is warranted before generalities are proposed, these results highlight the importance of considering the possibility of any front type in any type of estuary. This is especially important in remotely sensed or modeled locations where in situ data may be scarce, and where activities such as dredging or shoreline development are considered for an estuary. The successful use of Froude angle analysis on field data is an exciting development for the potential prediction of the location and orientation of fronts in an estuary. Further analysis and model simulation is certainly warranted. In particular, use of such computational methods to predict the type of front from the pattern of information vector convergence may prove useful to coastal planners considering such activities.

THIS PAGE INTENTIONALLY LEFT BLANK

IV. SUMMARY AND FUTURE DIRECTIONS

Densimetric intrusion fronts occur in broad, well-mixed estuaries both simulated and in situ, despite generalizations to the contrary. Though lateral expansion of the waterway occurs in both cases, the sill or bathymetric break is the facilitator in the generation of downslope gravity currents and surface convergence fronts. Front prediction and characterization techniques based on non-dimensional Froude number calculations are developed in this research that are of great value to operational planners in the littoral battle space or policymakers in coastal regions.

A. MODEL SIMULATIONS OF TIDAL INTRUSION FRONTS IN AN IDEALIZED BASIN

The idealized hydrodynamic model domains studied here are designed to examine tidal intrusion fronts in a broad, shallow estuary that would be considered well- to partially-mixed. The flow and density structures are examined to evaluate the forcing relationships associated with the observed features. Force balances between inertia and buoyancy (Froude numbers) remain the most straightforward means of evaluating tidal intrusion fronts and reveal insight into frontogenesis mechanisms of tidal intrusion fronts.

Delft3D-FLOW resolves tidal intrusion fronts and is appropriately sensitive to variations, resulting in tidal straining or location shifts when ΔS varies. Resolution is sufficient to show finer details of the intrusion as well, such as dissipation features behind the leading edge of the intrusion. Force balance irregularities along the lateral margins of the SWP (e.g., Figure 7e,h) hint at elevated flow velocities in the model that would be characteristic of these regions [*Lowe et al.,* 2002].

Structural evolution indicates that downslope gravity currents form almost instantaneously near the centerline, generating surface subduction at the supercritical slope break. Lateral expansion along the expansion envelope begins once the SZ reaches equilibrium near the SWP leading edge. The PF slows its advance, but expands laterally as the subsurface gravity current advance accelerates, likely facilitated by the residual deep stratification. The SZ may be decoupled from the gravity current, requiring individual attention in the future to fully understand. The toe of the intrusion is consistent with the behavior of the intrusion "head" from previous laboratory experiments [*Lowe et al.,* 2002; *Gristenko and Chubarenko,* 2010]. The intrusion toes are active up-estuary of an active SZ and PF. Density structures and surface gradients are the most definitive PF locator, as expected for a hydrodynamic model study, but F^2 and F_Δ^2 are also good diagnostics. Contrary to *Thain et al.* [2004], however, F_Δ^2 does not show the best PF alignment. Rather, F^2 lined up most reliably, has the added utility of describing the SZ's subsurface extent, and may even be able to distinguish actively advancing regions of the front. Composite Froude number G^2 shows limited use in determining front location. Structure, flow, and force balance relationships are observed laterally in an equivalent sense to the longitudinal dimension, but at much smaller length scales, necessitating the employment of two-dimensional techniques to evaluate frontogenesis and hydraulic control mechanisms.

Calculation of critical plunge width b_p and depth h_p as a coupled system rather than independently allows for evaluation of whether the intrusion front is released from hydraulic control by expansion or depth, or a combination of the two. For the cases in this study, a clear distinction is evident between the fronts in depth and expansion released basins. Shallow, expansion controlled bathymetries generate broad, crescent shaped fronts that quickly reach dynamic equilibrium and then expand laterally. Depth controlled basins produce V-shaped fronts that advance more rapidly but take longer to attain dynamic equilibrium, and thus do not expand laterally. SWP expansion in a narrow basin quickly reaches the sides and limits evaluation to the longitudinal dimension only.

Froude angle rotations evaluate how expansion and depth information is transmitted to and influences the plunge front. Plunge envelopes appear to be the principal information pathways determining the dynamic equilibrium position of the front. The slope break envelope contains the frontogenesis mechanism, but constrains the lateral extent of the front until it reaches the expansion envelope, which allows it to expand laterally while the slope break envelope continues to influence the shape of the central, partially depth controlled PF segments. The leading edge of the slope break envelope defines the portion of the front that advances forward, but where the PF extends along the expansion envelope, it becomes informed by expansion, and advancement will have a lateral component. In a basin where control is released by depth, the front takes longer to reach the dynamic equilibrium of the plunge envelope, limiting the opportunity for lateral expansion, which is also limited by the narrowness of the expansion envelope. This newly understood composite control mechanism could have implications on the impact assessments for anthropogenic “improvements” to an estuary.

Although the general differences between expansion and depth control are shown in this analysis, the exact details are not explicitly enumerated in this study. The precise nature of the bathymetric sensitivity should be examined in greater detail if these techniques are to be employed as a planning tool. Quantitative scales and relationships are left out of this analysis in favor of general comparisons due to the extreme generality of the model domain and known limitations of the model physics.

The two-dimensional hydraulic control evaluation techniques used in this study demonstrate how changes in the bathymetry can change the character of a convergence front by altering its control mechanism. Consider an estuary that has not been dredged for some time, allowing sediment to build up within a central channel. Dredging a channel through the shoal and/or basin could quickly change the hydraulic control and/or release mechanism, reorienting and relocating the intrusion fronts significantly, along with sediment, larval, and pathogen pathways, navigational hazard zones, and other secondary effects [*Ralston, et al.,* 2012]. The techniques and interpretations developed by this study may serve as a guide for engineers and scientists to apply to actual bathymetry and physical forcing in developing an assessment tool to understand the impacts of artificial “improvements” such as dredging or natural processes such as sea level rise to the dynamic equilibrium of estuarine systems.

B. STRATIFIED CONFLUENCE FRONTS IN A SHALLOW COASTAL PLAIN ESTUARY

A densimetric intrusion front is described in a well-mixed estuary. To facilitate this unique feature in an unexpected setting, artificial dredge spoils islands segregate

Traps Bay from the main central channel. This allows production of a persistent mid-density water mass as lower-density estuary water and high density ocean water trade input pulses that get sequestered and mixed in Traps Bay due to lower velocities and long residence times. This mid-density water is then consistently brought into confluence with intruding ocean water during flood tides. Because the convergence occurs in the lee of a shoal that imposes hydraulic control on the dense water flow, the oceanic intrusion is able to subduct beneath the mid-density Traps Bay water as a densimetric intrusion. The front structure is typical of a tidal intrusion front in most aspects, although it is oriented obliquely to the primary ocean flood flow. The confluence is also problematic as it allows minimal shear to develop, keeping the flow supercritical on both sides of the front. This is expected in a well-mixed estuary, but not conducive to formation of an intrusion-type front. The balance orientation of the front is derived using Froude angles to re-calculate front-normal Froude numbers to define the supercritical to subcritical transition expected in the standard view of tidal intrusion fronts.

Stratified intrusion fronts have never before been documented in such a shallow, well-mixed estuary, nor have intrusion-type features been documented in flow patterns other than convergence in near perfect opposition. It is proposed that the bathymetrically-induced confluent subduction observed here is a subset of the broader tidal intrusion front category, or a hybrid front type of axial convergence front, which may help to explain how the front may be able to gradually transition to that type of front farther up-estuary as suggested by the Delft3D model simulation. Key to this type of confluent frontogenesis mechanism, however, is a supporting mechanism that allows a mid-density water mass to form in a side bay or similar lateral location separated from the main flow by shoals or islands. In NRE, the dredge spoils provide the flow separation to allow mid density water to form in Traps Bay, and the shoal deposited near a bend in the central channel provides the hydraulic control near the re-convergence to induce the subduction.

Though the estuary circulation vs. mixing classifications of *Hansen and Rattray* [1966] are understood to potentially vary locally (temporally and spatially), these generalizations are nevertheless used to draw estuary-wide conclusions from remote sensing or model data when in situ data is scarce. The observed generation of an intrusion-type front in what is classified a well-mixed estuary, despite its irregularities, should give pause to coastal scientists and engineers who place great importance on such estuary-wide classifictions. Rather than a transitory vertical mixing zone, the stationary front observed is more likely to inhibit vertical mixing in the stratified portion in favor of the surface subduction and intrusion head regions. This in turn creates well-defined constituent pathways and boundaries, as well as sediment erosion and deposition zones that when repeated every flood tide could lead to unintended or unwanted migration or generation of channels and shoals.

Though further exploration of well-mixed estuaries is warranted before generalities are proposed, these results highlight the importance of considering the possibility of any front type in any type of estuary. This is especially important in remotely sensed or modeled locations where in situ data may be scarce, and where activities such as dredging or shoreline development are considered for an estuary. The successful use of Froude angle analysis on field data is an exciting development for the potential prediction of the location and orientation of fronts in an estuary. Further analysis and model simulation is certainly warranted. In particular, use of such computational methods to predict the type of front from the pattern of information vector convergence may prove useful to coastal planners considering such activities.

C. FUTURE DIRECTIONS

The Froude angle analyses developed in the idealized model analysis and validated in the field observations provide useful tools for predicting the location and character of estuarine fronts. This could prove useful to organizations such as the Naval Oceanographic Office (NAVO) who perform environmental reconnaissance with remotely sensed data and little else. Further utility will be made possible once the NRE model domain is fully operational. Comparisons of observed front location and character will be performed to assess the full utility of model simulations in predicting estuarine front behavior. Included in this assessment will be an evaluation of the potential for computational techniques to discriminate the front type as well as location. Front type allows further interpretation of processes such as sediment transport and vertical mixing.

To accomplish these assessments, however, additional two-dimensional flow computations will be evaluated.

Vector analyses are frequently used to describe the circulation patterns in a multi-dimensional flow field. Flow patterns in steady state velocity fields can be described with such time-independent techniques as streamline analysis or Vector Field Topology (VFT), which interprets particle trajectories by integrating velocity stream lines in 2D or stream surfaces in 3D to compute stable (convergent) and unstable (divergent) flow manifolds. While useful, the instantaneous velocity snapshots used in these analyses are an important drawback if considering unsteady flow fields such as tidal environments [*Sadlo and Peikert*, 2007].

For an unsteady flow field, the Lagrangian Coherent Structures (LCS) concept separates a flow into regions exhibiting similar behavior [*Haller*, 2001] with finite-time Lyapunov exponents (FTLE). FTLE is a measure of the distortion neighboring particles undergo over a pre-determined ("finite") period of time. Different from a particle trace, FTLE integrates the time-dependent particle trajectories in either backward or forward time and compares the distortion of the final particle positions to the baseline of the initial positions. Thus the FTLE field describes the degree to which particles are attracted (backward FTLE) or repelled (forward FTLE) from each other. LCS boundaries are then described with maxima or ridges in the FTLE fields.

Conceptually, the repelling LCS ridges can be viewed as defining the most likely source regions and the attracting ridges interpreted as the locations to which particles will most likely end up. When flow and particle concentrations are induced geographically, such as through a constriction, these interpretations are strengthened, and using a meaningful integration time, can serve to confidently visualize the flow boundaries. In an estuary with a constricted inlet such as NRE, it may therefore be reasonable to view LCS as a method of defining the boundaries of the tidal excursion. Furthermore, the same morphological complexity that separates the NRE into distinct water masses [*Sheets*, 2013] can assist in visualization of those water mass boundaries and how they vary through the tidal cycle.

Analyses are underway to assess circulation patterns in the NRE with FTLE to describe the origin and fate of oscillating tidal flows. Additionally, water mass boundaries may be defined that correspond to the location of the fronts described in Chapter III. Critical in these analyses is finding the most appropriate and physically meaningful integration time, which has yet to be determined. Early results are encouraging, and the hope is that this will yield yet another technique to predict and characterize estuarine fronts with numerically simulated data.

THIS PAGE INTENTIONALLY LEFT BLANK

TABLES

Effect	Basin		Ocean		River			M_{2b}/M_{2o} (%)	ΔS (psu)
	shape	bathy	M_{2o} (cm)	S (psu)	Δ (cm)	α (°)	M_{2b} (cm)		
Depth	open	baseline	50	34	3	68	18	36	-3
	open	shallow	50	34	3	68	18	36	-3
	open	close	50	34	3	68	18	36	-3
Width	narrow	baseline	50	34	2	64	18.5	37	-8
	narrow	shallow	50	34	2	64	18.5	37	-8
	narrow	close	50	34	2	64	18.5	37	-8

Table 1. Table 1: Model domains and boundary conditions. Basin shapes and bathymetries for each simulation (see Figure 3). Ocean boundary forcing remained constant. River forcing was selected to maximize tidal intrusion front formation while retaining stability. Salinity depression was calculated through the plunge depth and width calculations (Eq. 2-3). All other boundary conditions and parameters were constant throughout the study.

<table>
<tr><th></th><th><u>May 8</u></th><th><u>May 9</u></th><th><u>May 13</u></th></tr>
<tr><td>Mini-cat</td><td colspan="2">28 hr</td><td>5 hr</td></tr>
<tr><td>Locations</td><td colspan="2">M081
M082
M083
(Figure 3, 6)</td><td>M131
M132
M133
M134
(Figure 3)</td></tr>
<tr><td>ADCP interval</td><td colspan="2">1 min</td><td>1 min</td></tr>
<tr><td>CTD</td><td colspan="2">X (M083 in Figure 8)</td><td>X (Figure 8)</td></tr>
<tr><td>CTD casts</td><td></td><td>Single transect, 10-20m spacing @ 15 min intervals (Figure 5, 6)</td><td>Transects + Dispersed field (Figure 5, 9)</td></tr>
<tr><td>Boat-mounted CTD</td><td></td><td>Transect, 10-20m spacing @ 15 min intervals (Figure 5)</td><td></td></tr>
<tr><td>UUV</td><td></td><td>Surface survey (Figure 5)</td><td></td></tr>
<tr><td>Drifters</td><td></td><td></td><td>9 x 5 releases (Figure 7)</td></tr>
<tr><td>Visible</td><td></td><td>GPS trace (Figure 3,5,7,10)</td><td>Field notes</td></tr>
</table>

Table 2. Summary of instrument deployments discussed in this paper. Top section refers to mini-cats, middle to water quality measurements from small boats, bottom to accessory front measurements. Figures showing location or results are noted where applicable.

FIGURES

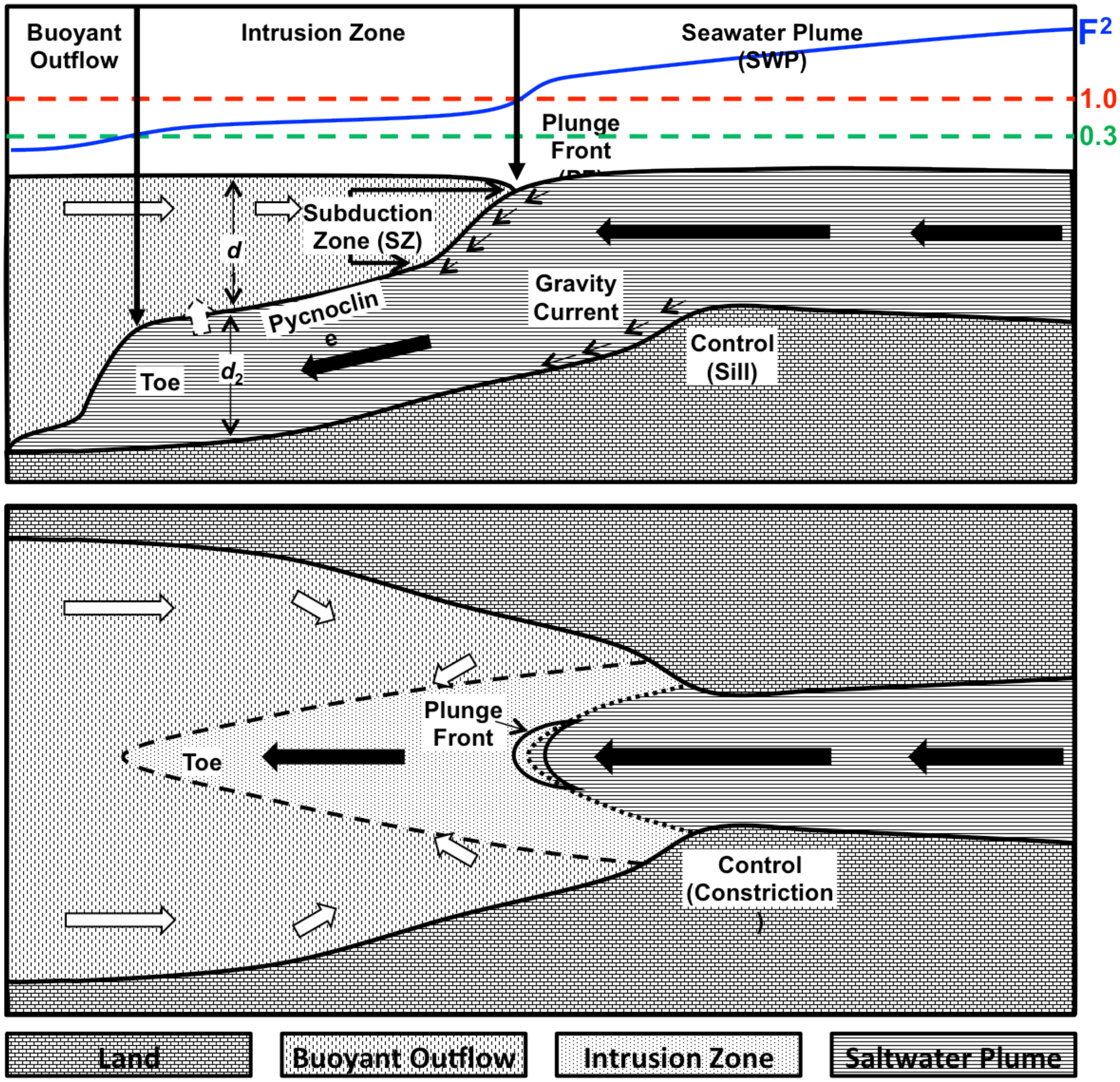

Figure 1. Conceptual model of tidal intrusion fronts in (a) profile and (b) plan view. Black arrows represent the oceanic flood originating from the right of the figure. Terminology used in this paper, including water bodies, dynamic zones, and structural features, are labeled for reference. Idealized Froude balances are traced in blue. Dashed lines denote the supercritical (red) and subcritical (green) thresholds for a two-layer system. [After *Largier*, 1992].

Figure 2. **(a)** New River Estuary, NC. Model domains used in this study are inspired by the dimensions, geomorphology (lagoon-type) and dynamics (well-mixed) of this basin. **(b)** Close up showing blue ocean water intruding into the brown water of the New River Estuary, and the fronts that form at the interface. [From *Google Earth*, 2013].

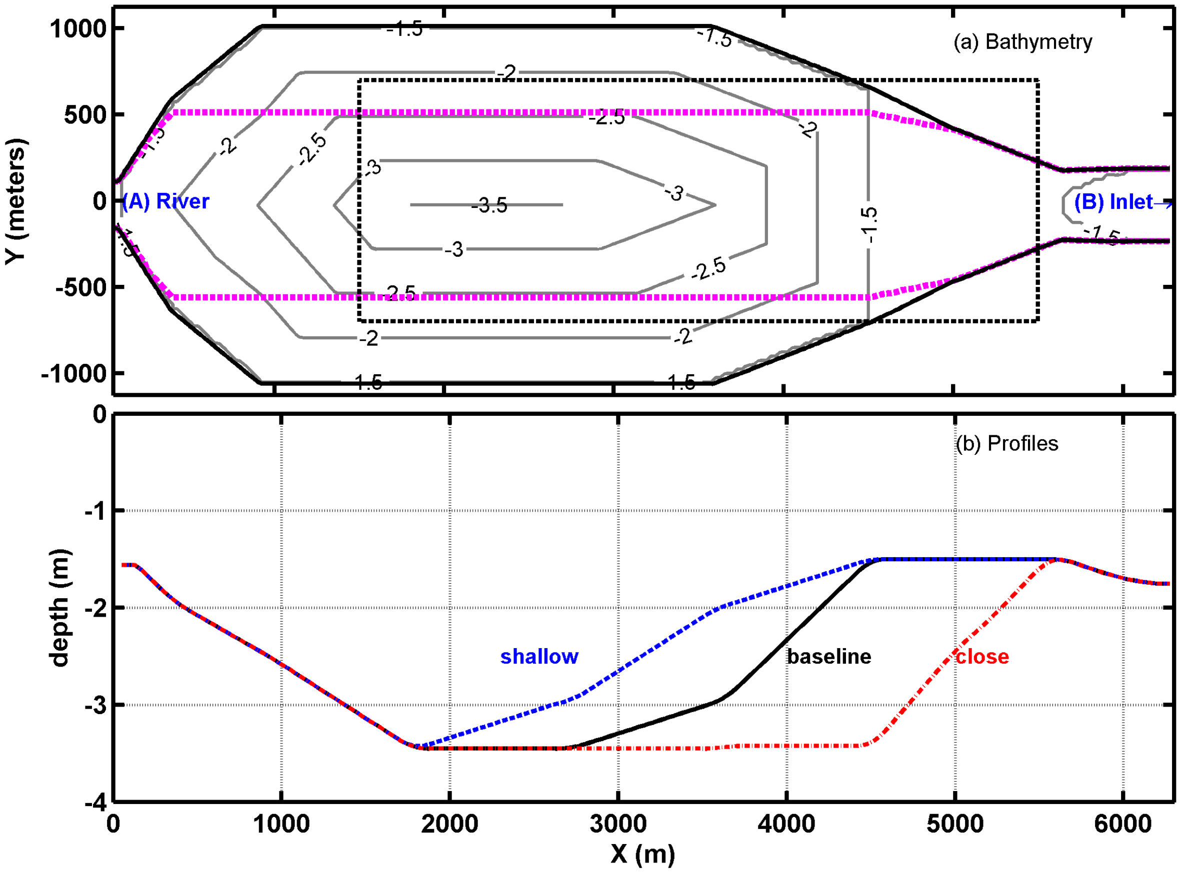

Figure 3. **(a)** Model domain of the "open" type basin with the baseline bathymetry contoured every 0.5 meters. The left hand side of the figure is the model boundary, with the river input defined as the boundary condition at (A). The open ocean model boundary is 4km beyond the right hand side of the figure (B). Tidal flood flows in all model runs move right to left, referred to as the "upstream" or "up-estuary" direction. Use of "up flow" or "down flow" in the text refers to the *dominant* tidal flow direction. For ease of analysis, map depictions cover only the area outlined by the black dashed box. The dashed magenta line is the outline of the "narrow" basin type. **(b)** Centerline profiles of the baseline (black solid), shallow slope (blue dashed), and close slope (red dot-dash) model bathymetries.

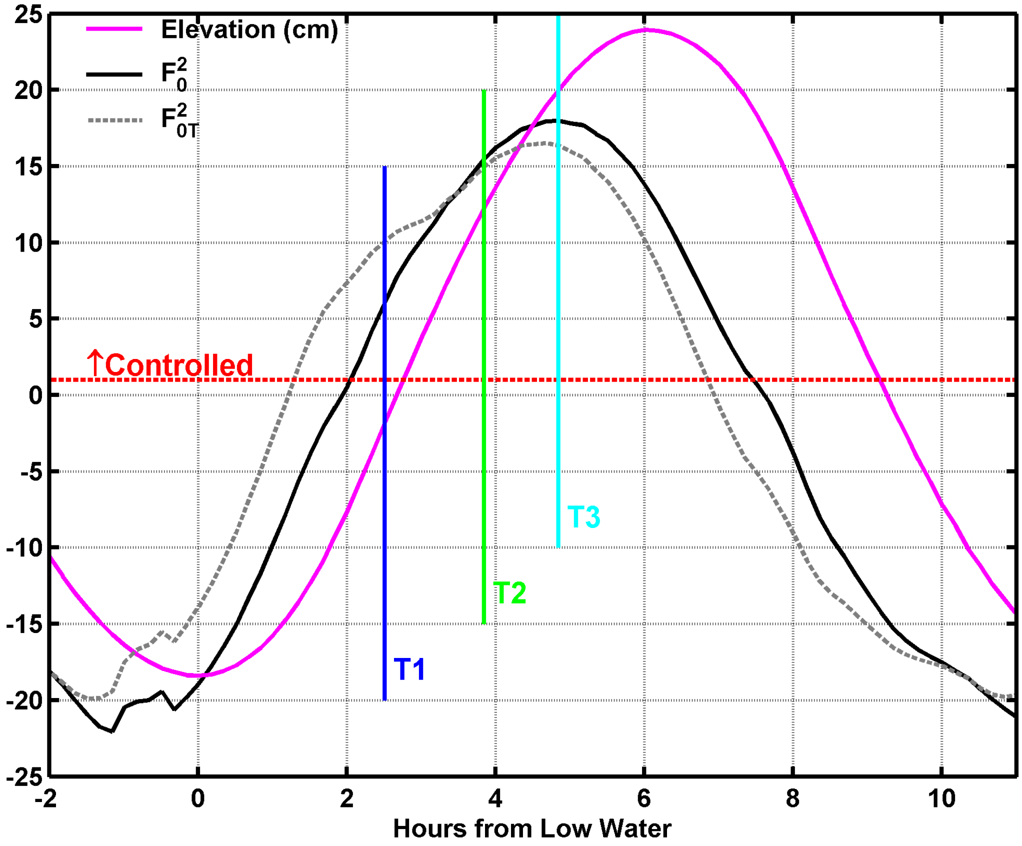

Figure 4. Basin Input Froude number components (inlet in black, total=inlet+river in gray dashed) plotted against tidal elevation at the inlet constriction (magenta) over a complete tidal cycle. Input Froude number, calculated by $F_0^2 = {}^{|Q_0|Q}\!\big/_{g' h_0^3 b_0^2}$ is used here as a proxy for velocity since $Q_0 = u_0 h_0 b_0$. Positive values are into the basin. The red dashed line marks a critical ($F^2 = 1$) force balance. Analysis times are shown as vertical lines.

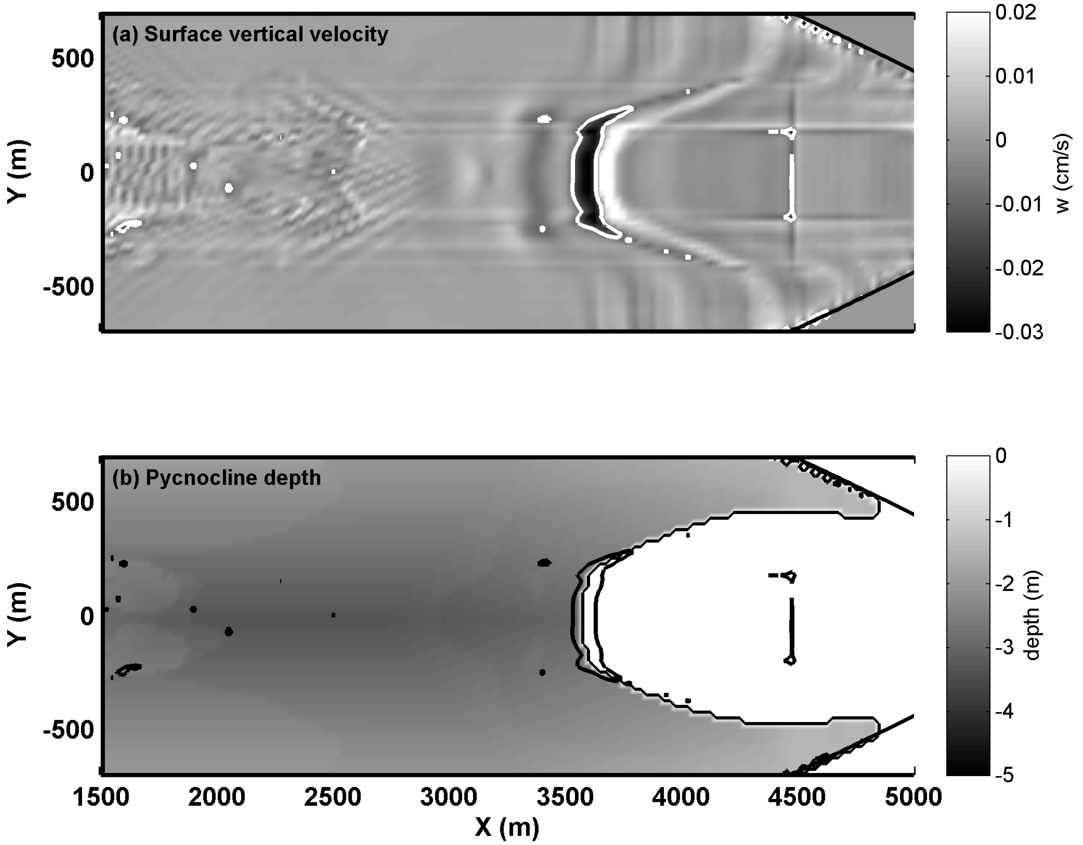

Figure 5. Comparison of surface front evaluation techniques. **(a)** Surface ($\sigma 1$) vertical velocity at T2 (mid flood) for the baseline basin geometry. Downward velocities are plotted in the darker shades, with $w \leq -0.01$ cm/s, defining the plunge front (PF) assumed to correlate to the presence of a foam line, outlined in white. **(b)** Pycnocline depth d_1 is plotted, outlined at $d_1=0$, and overlain by the PF. The $d_1=0$ outline marks where the pycnocline intersects the surface as a density front, marking the edge of the seawater plume (SWP). It aligns with the PF where present. Weaker downward velocity patterns outside of this contour are not considered to follow the shape of the SWP.

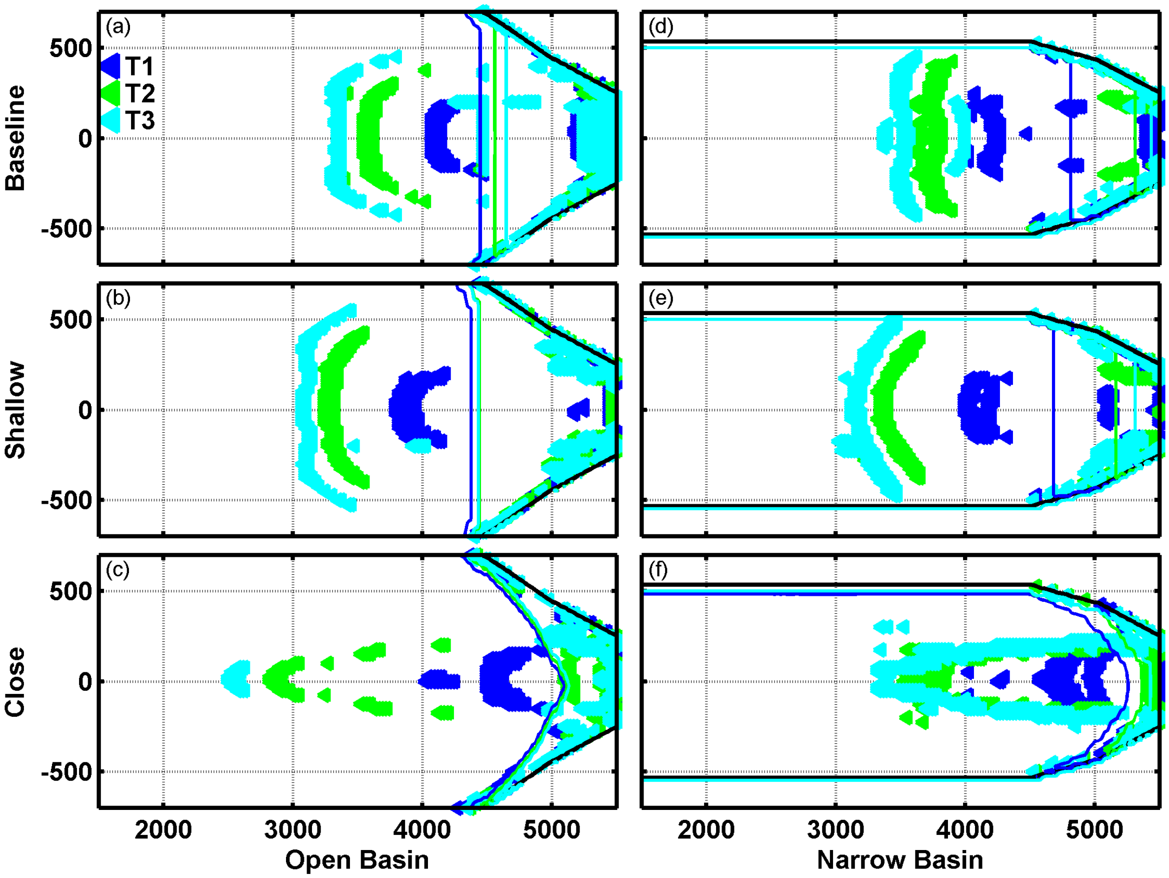

Figure 6. Plunge front progression through the analysis times (◀**T1**, ◀**T2**, ◀**T3**) shown in Figure 4, for all model domains. Triangles mark all model grid points with *w*≤-0.01 cm/s in the surface level, *σ1*. Solid lines representing the calculated plunge section (Eqs. 2 & 3) are colored accordingly. Although changing the slope (baseline (a) and (d) vs. shallow (b) and (e)) does not significantly change the character of the plunge front or plunge section, a much different character and evolution develop when the slope break is moved closer to the inlet ((c) and (f)).

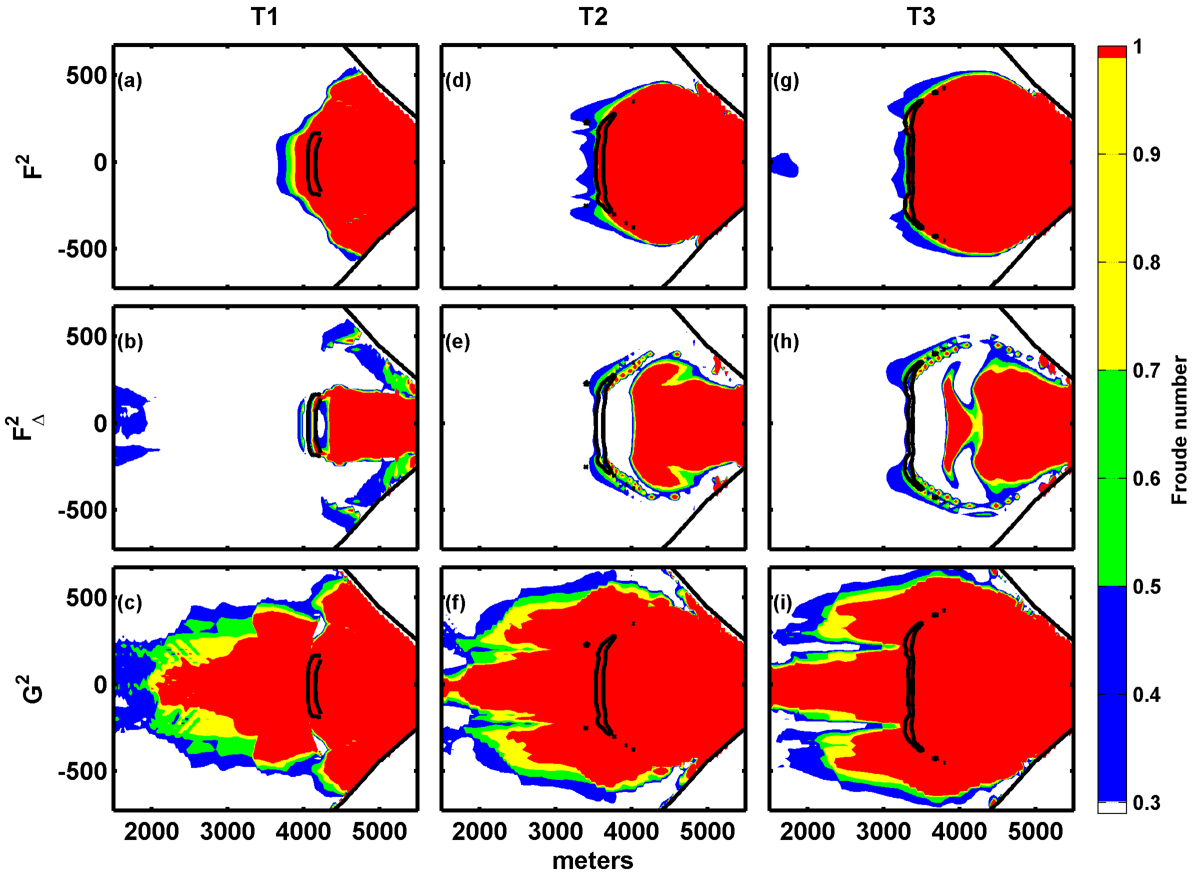

Figure 7. Plan view plots of the computed Froude balances (F^2, F_Δ^2, G^2) at each analyzed time step (T1, T2, T3) for the baseline bathymetry. Color fill is the force balance, where $F_i^2 \geq 1$ (supercritical) is red, and the cooler colors are scaled to the critical range $0.3 \leq F_i^2 < 1$. Subcritical areas are white. Plunge fronts are shown for comparison in each plot.

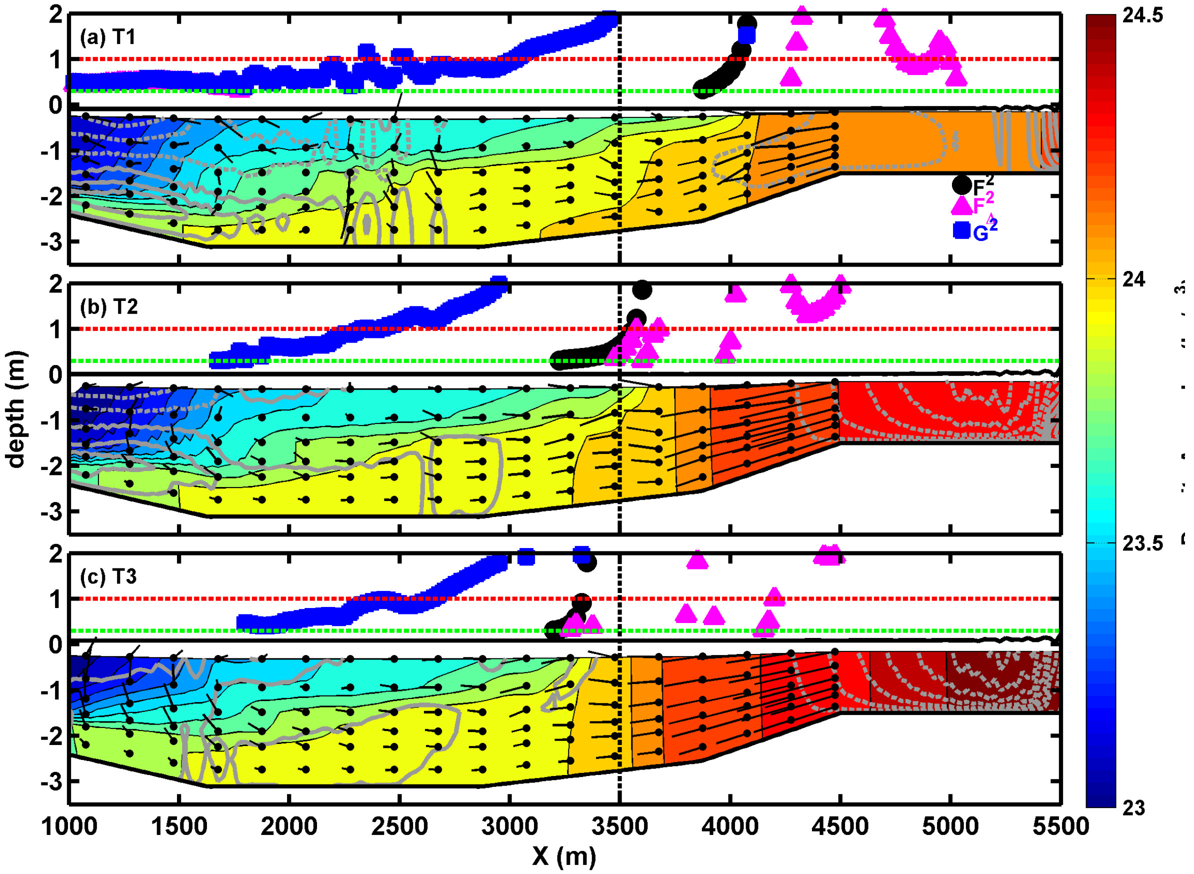

Figure 8. Longitudinal profiles plotted 175 meters from centerline in the baseline bathymetry for **(a)** T1, **(b)** T2, and **(c)** T3. Color filled contours are density with a 0.1 kg/m^3 interval. Velocity vectors are plotted as black lines emanating from dots at the grid points. Grey contours are lateral velocity along the section (solid + / dashed -). Corresponding Froude numbers (●F^2, ▲ F_Δ^2, ■G^2) are plotted above each grid point, with dashed lines marking the supercritical (red) and subcritical (green) transitions. The vertical black line marks the intersection of transverse profiles in Figure 9.

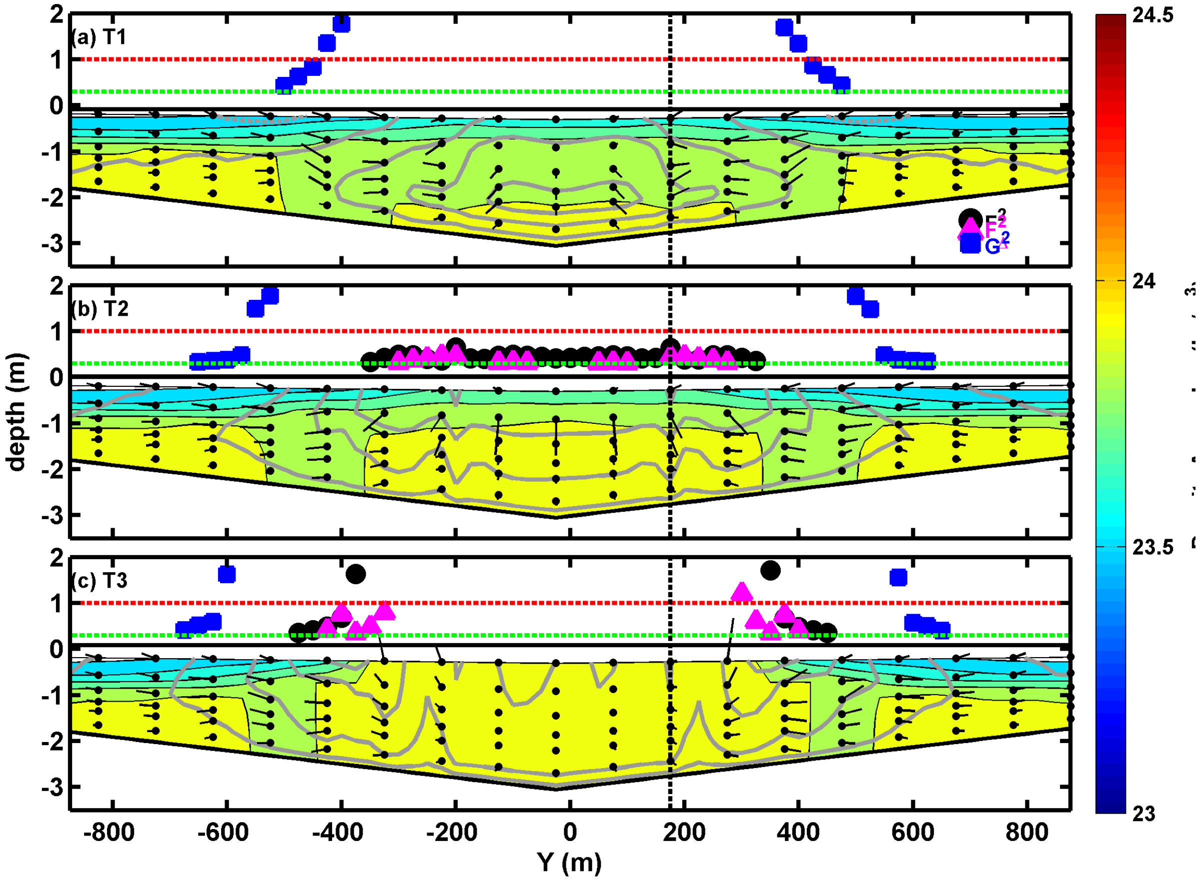

Figure 9. Transverse cross-sections at x=3500 m, 2000 meters up-estuary of the inlet (x~5500) in the baseline bathymetry for **(a)** T1, **(b)** T2, and **(c)** T3. Figure markings are identical to Figure 8. The vertical black line marks the intersection of transverse profiles in Figure 8. Contours of the streamwise velocity (solid contours are up estuary) show the subsurface velocity maxima associated with the initial intrusion of the deep layer toe (a). This maximum rises to the surface as the plunge front passes (b), and then eases as the tidal acceleration slows and the barotropic flow becomes friction-dominated (c).

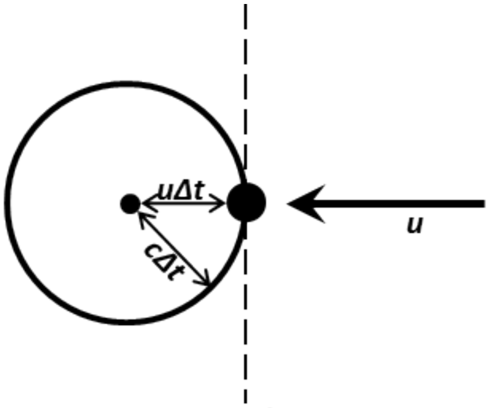

a) Critical flow

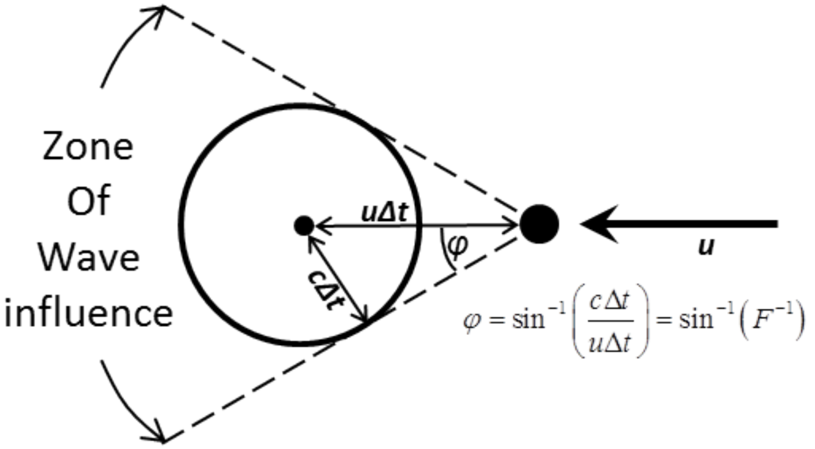

b) Supercritical flow

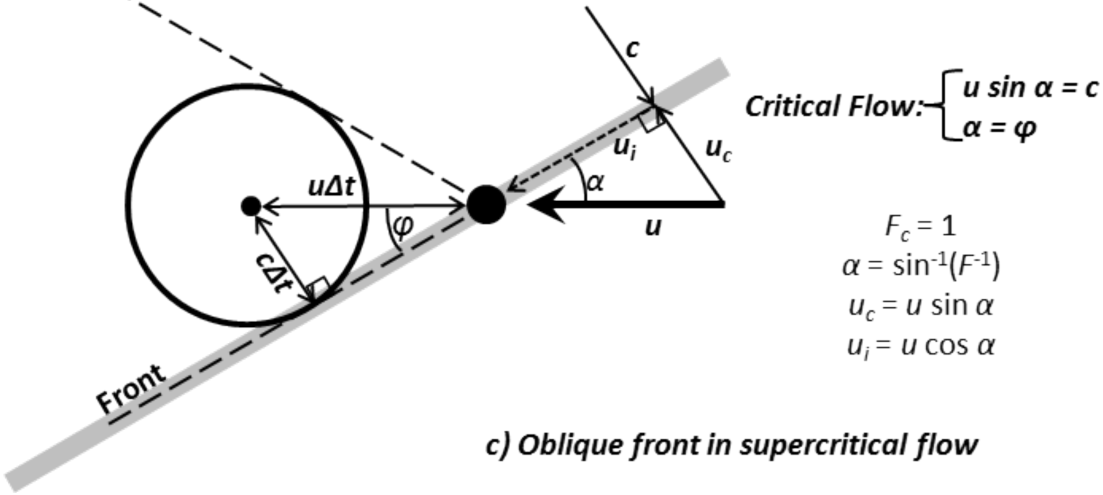

c) Oblique front in supercritical flow

Figure 10. Propagation of wave fronts for critical **(a)** and supercritical **(b)** flow, and critical conditions for an oblique front in supercritical flow **(c).** In all cases a flow with velocity *u* flows from right to left, and an instantaneous disturbance is initiated at the large black dot. **(a)** Critical flow is where the wave speed of the fluid, $c=(g'h)^{1/2}$, is equal to *u*, and the right-hand edge of the wave field forms a stationary wave at the disturbance but propagates to the left

elsewhere. **(b)** In supercritical flow, $u>c$ and the entire wave packet detaches from the disturbance in the direction of the flow u. The envelope containing information on the wave is described by the Froude angle φ, as shown. **(c)** Supercritical flow represented as critical relative to a two-dimensional front when the Froude angle φ is equal to the angle of inclination between the front and the oncoming flow, α. In this case, a Froude number calculated using the velocity component normal to the front, shown as $u_i = u \sin \alpha$ opposing c perpendicular to the front, is equal to 1 and called the "critical vector". The dashed line depicting the residual component u_i is called the "information vector". [After *MacDonald and Geyer*, 2005].

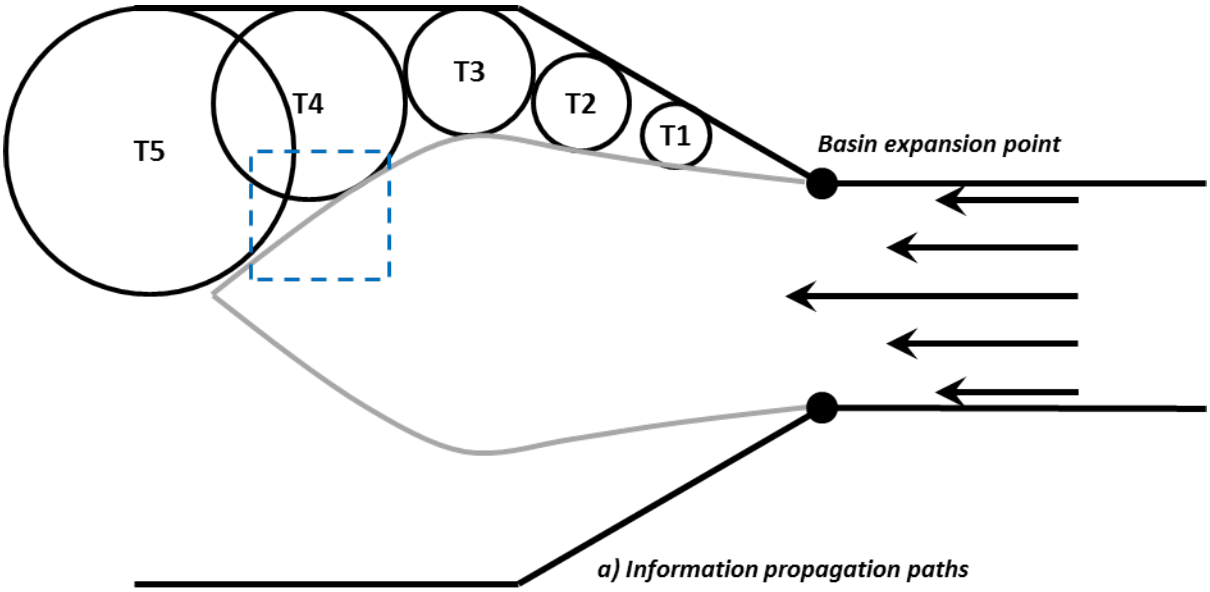

a) Information propagation paths

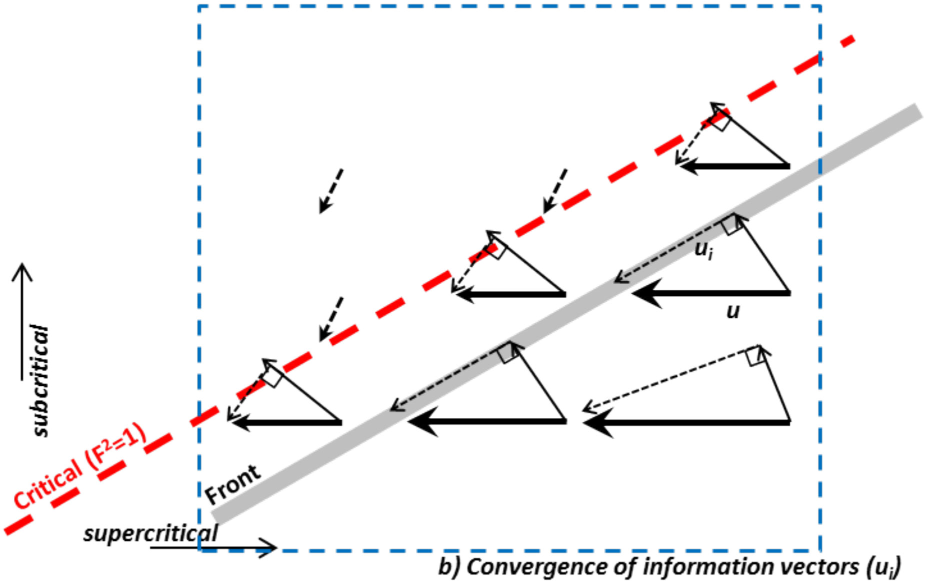

b) Convergence of information vectors (u_i)

Figure 11. Depiction of information flow in the analyzed domains. **(a)** The point of

expansion from the inlet to the basin is deemed the disturbance, or information point (large black dot). The information of the expansion is advected and radiates from T1 to T5 as shown by the black circles. The associated information envelope is shown as the gray line. **(b)** Assuming the envelope also defines the front location, a spatially varying flow field within the dashed cyan box is shown by the dark arrows (solid = supercritical, dashed = subcritical). $\alpha = \sin^{-1}\left(F^{-1}\right)$ is calculated at each location and the critical and information vectors shown as thin solid and dashed arrows, respectively. This calculation is trivial for the subcritical region, and so information flows with the velocity vectors. Dashed information flow converges in all cases on the front location.

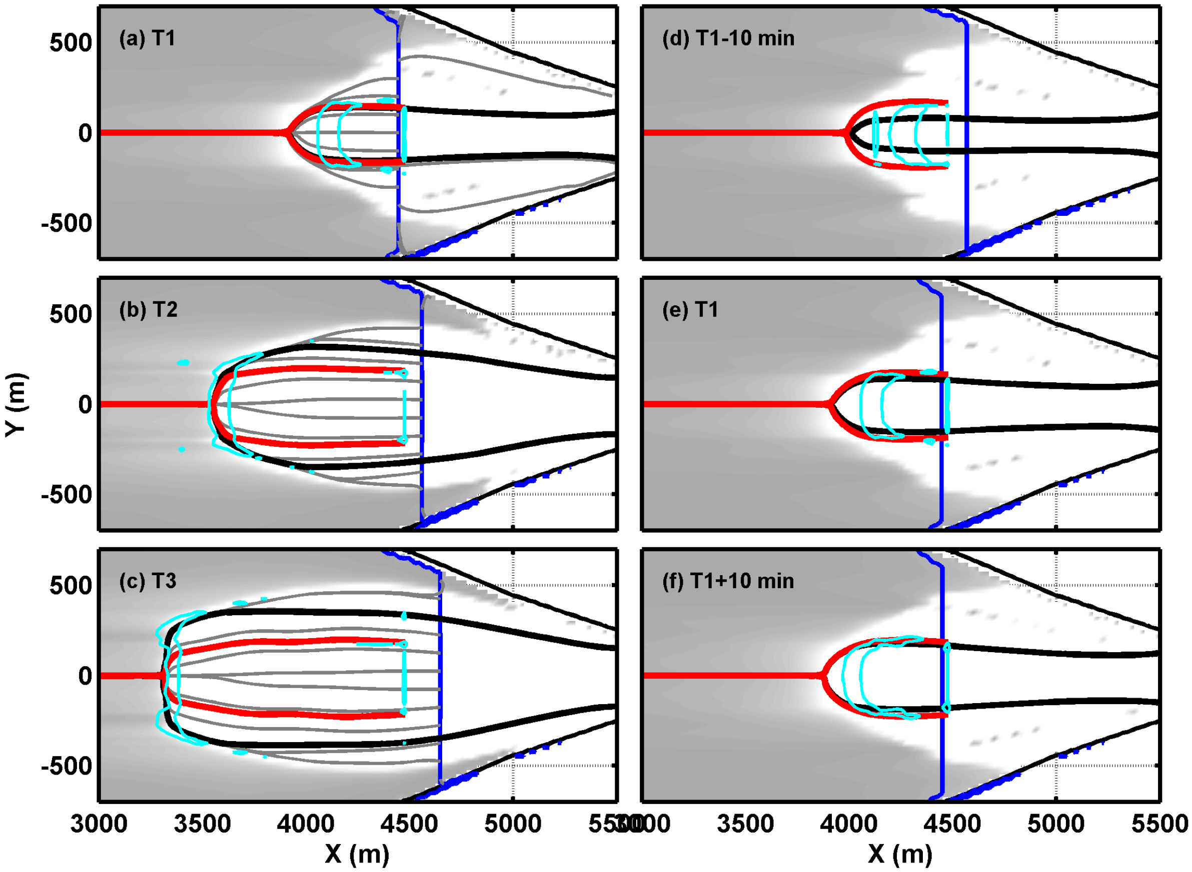

Figure 12. Information flow plots in the baseline bathymetry at the analyzed time steps **(a-c)** and individual time steps near the flood transition **(d-f)**. Black lines are expansion envelopes, and outline the region that is uninformed about the basin expansion. Red lines show the slope break envelope, and encompass the region containing slope break information. Gray lines are drawn from the calculated plunge section (drawn in blue) and indicate where the flow

contains information that the critical plunge criteria have been met. Cyan outlines depict the plunge fronts. Gray shading is $F^2<1$, where calculation of α is trivial.

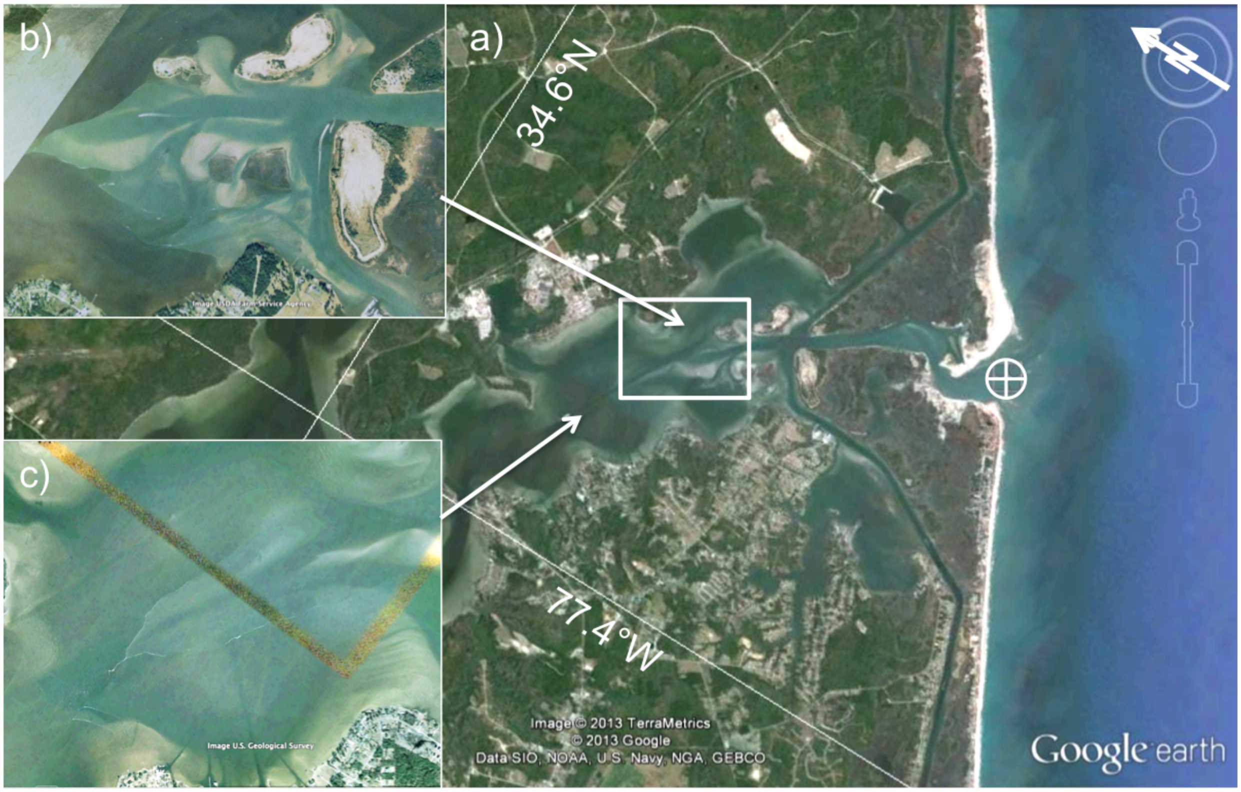

Figure 13. New River Estuary (NRE), North Carolina. **(a)** Latitude, longitude, and North references for the local 58° RIVET axis rotation are labeled in white. Cross hairs at the mouth of the inlet show the local coordinate origin. **(b)** Close up of flood tidal intrusion in main tidal channel, showing clear ocean water displacing dark, turbid estuary water. **(c)** Close up of V-shaped surface convergence front farther up estuary. [From *Google Earth*, 2013].

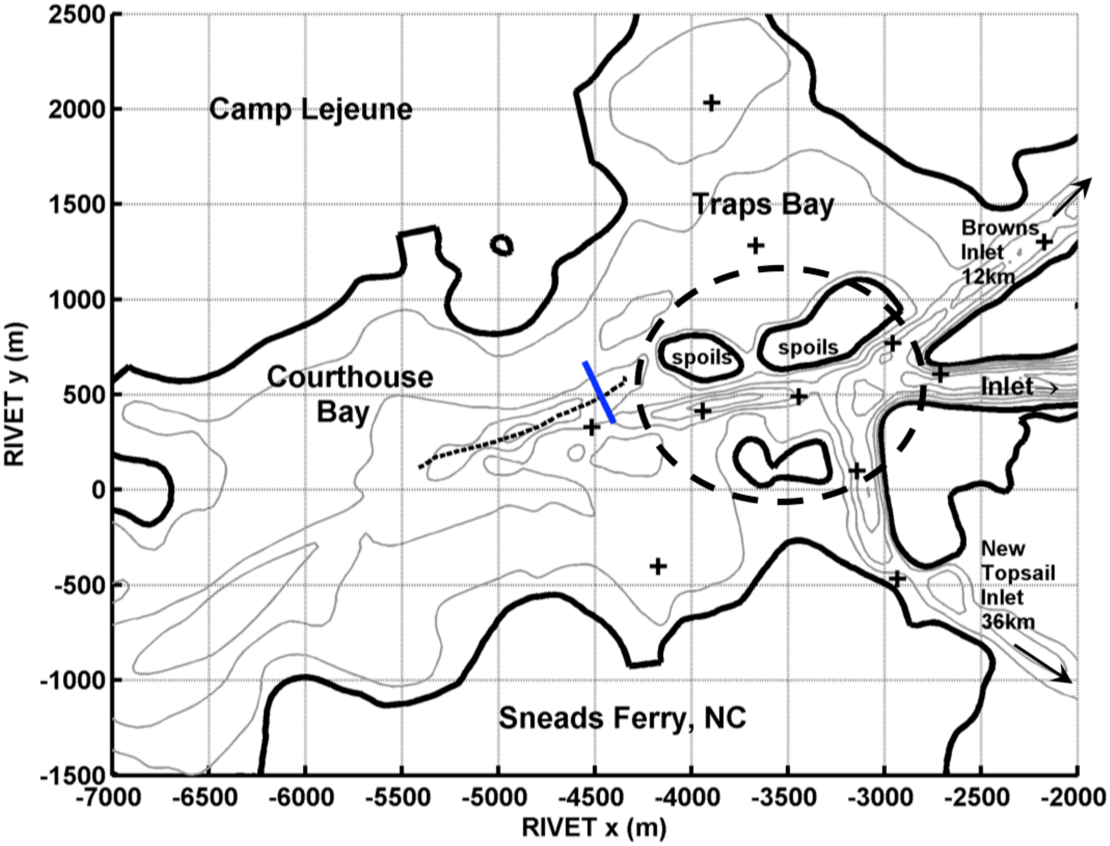

Figure 14. NRE bathymetry. Shoreline is shown as black heavy lines, bathymetry contours in gray (one meter intervals). Mini-cat deployment locations are depicted as (**+**). The dotted black like shows the front location and the heavy blue line shows the transect location as depicted in Figure 15. Dashed black oval highlights the artificially extended channel and dredge spoils islands. Coastlines and bathymetry are drawn from the corrected bathymetry used for the model simulation.

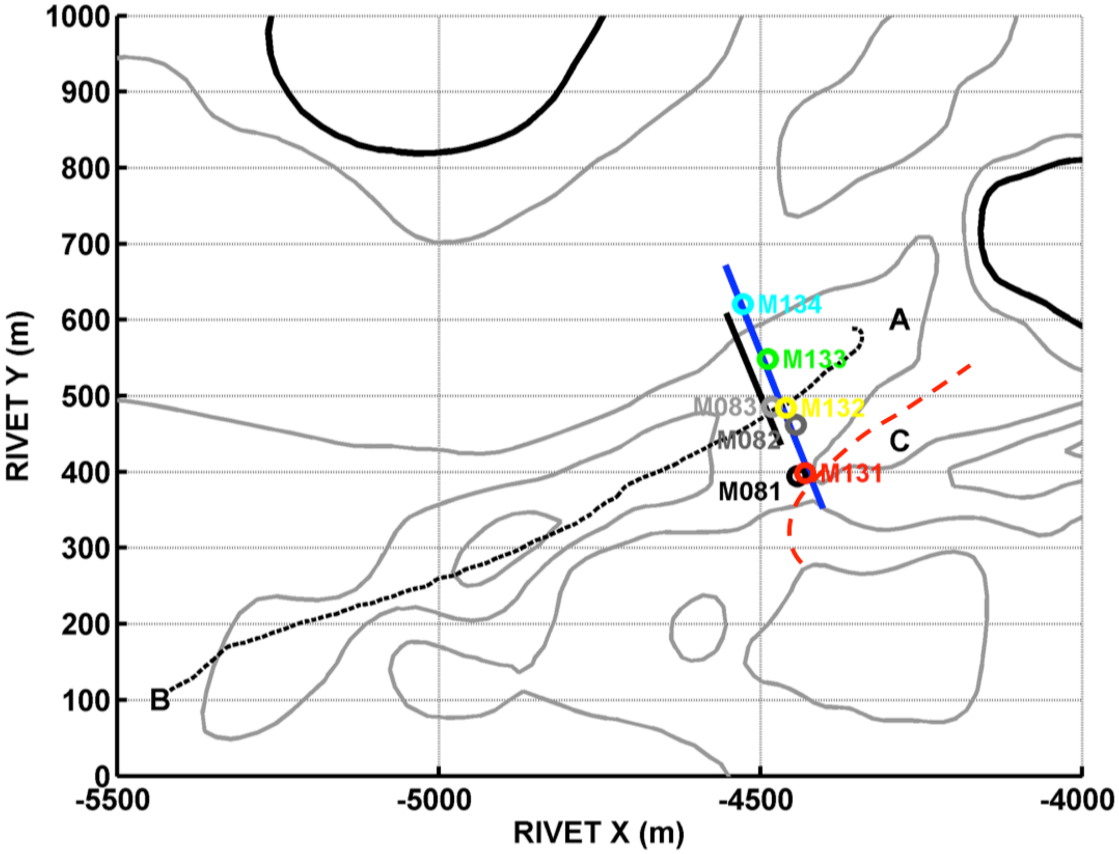

Figure 15. Mini-cats (○), transects (lines), and GPS surface front trace (dashed black line A-B) discussed in this paper. Front trace and blue transect line match those shown in Figure 14. Black and gray mini-cat locations were collected 08-09 May; colored locations on 13 May 2012. The red dashed curve marks the location of the sill at the intersection of the main tidal channel and the secondary channel that induces the front. Contours are 1 meter depth intervals.

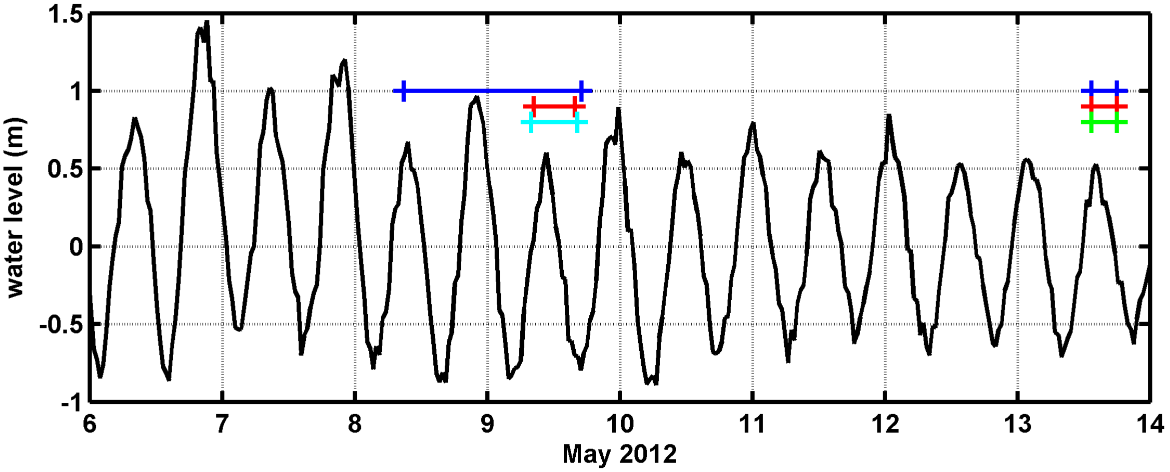

Figure 16. Offshore detrended tidal elevation during sampling periods (black). Deployment times are indicated by bars for mini-cats (blue), CTD casts and boat work (red), drifters (green) and UUV survey (cyan).

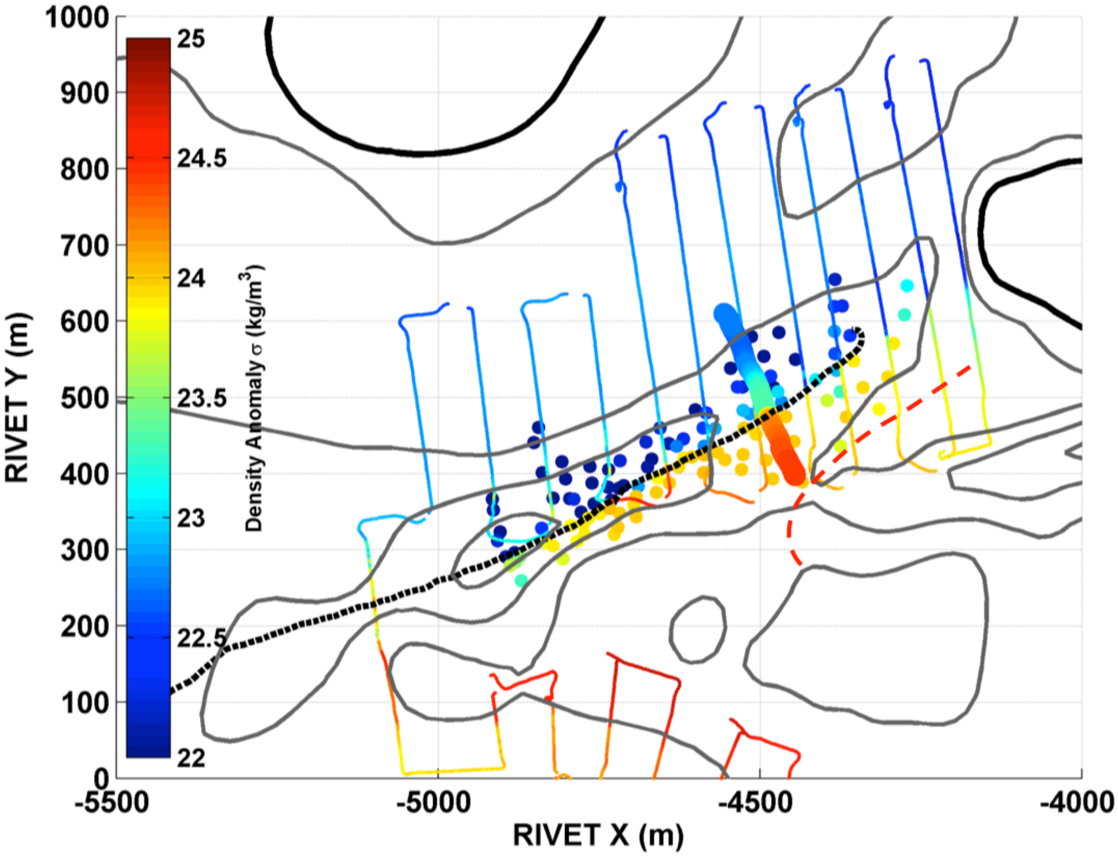

Figure 17. Front location summary. Measurements of salinity and temperature are colored by the surface density anomaly; thin colored line is the UUV survey on 09 May, large dots forming the wide colored line are from the CTD transects collected 09 May (see also Figure 18), scattered dots are surface densities from CTD casts collected 13 May. The dotted black line is the GPS track of the visual small boat trace of the front on 09 May. The red dashed curve marks the location of the sill (see also Figure 15). Contours are 1 meter depth intervals.

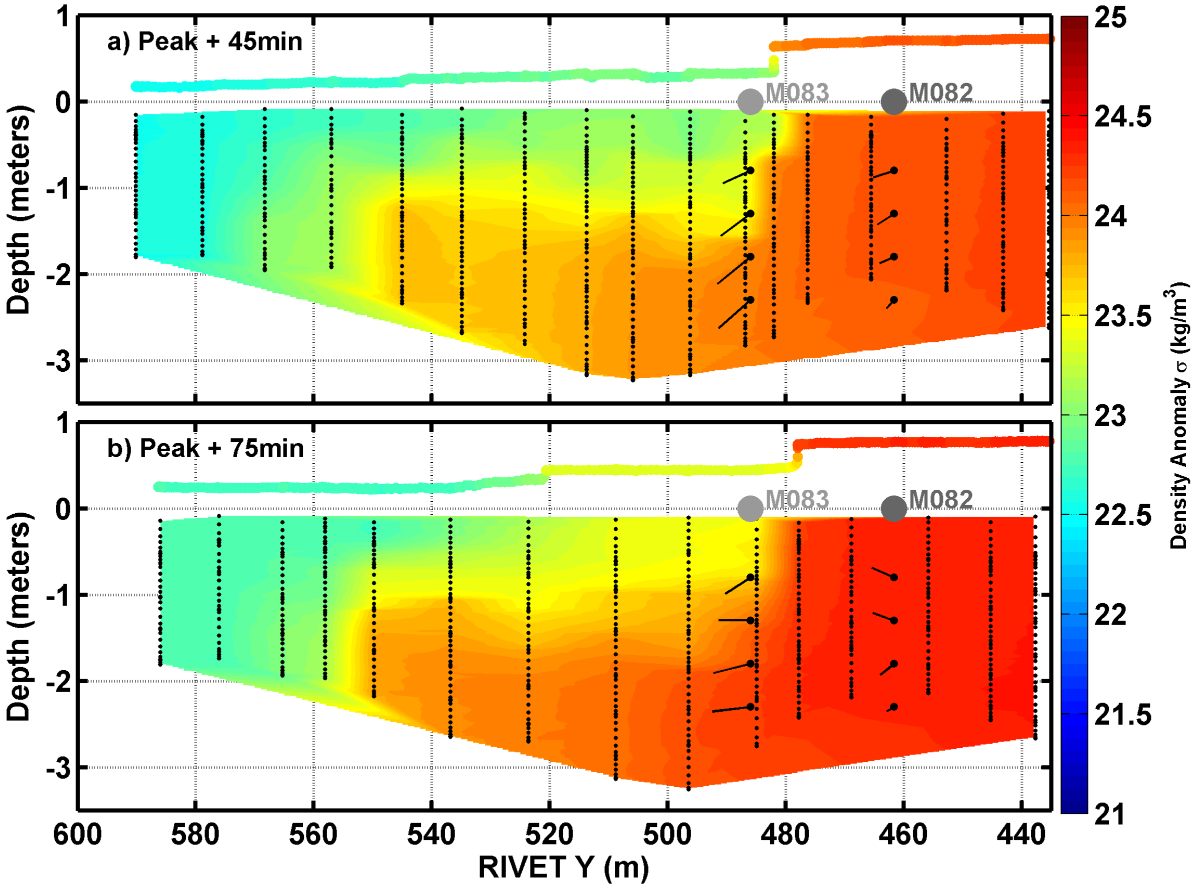

Figure 18. Detailed cross-sections of the front **(a)** 45 minutes and **(b)** 75 minutes after the offshore peak high tide on 09 May. Location is depicted in Figure 15 as the black line and Figure 17 as the wide colored line. View angle is seaward, with the central channel to the right and the exit of Traps Bay on the left. Color scale is density anomaly linearly interpolated between CTD casts shown as vertical black lines, collected sequentially right to left. Profile trace above each section shows the left to right trace of surface density immediately following the CTD transect. Velocity profiles at each mini-cat location are also shown as vectors.

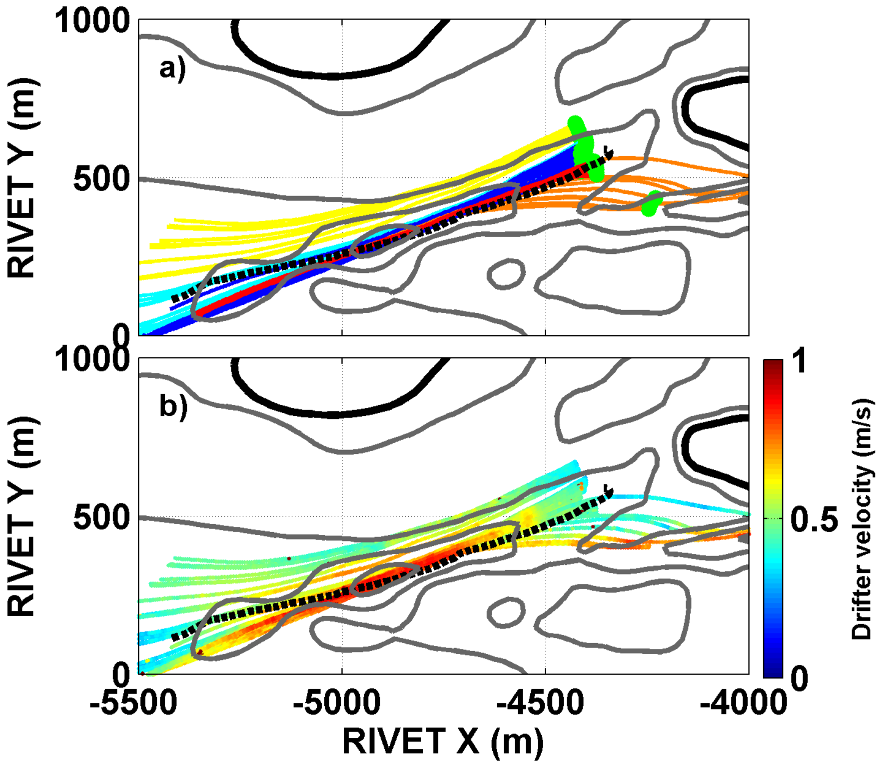

Figure 19. Drifter tracks on 13 May. **(a)** Colored by release group: 1, 2, 3, 4, 5, with green dots marking the drop locations. **(b)** Colored by velocity. The dotted black line is the GPS track of the visual small boat trace of the front on 09 May. Contours are 1 meter depth intervals.

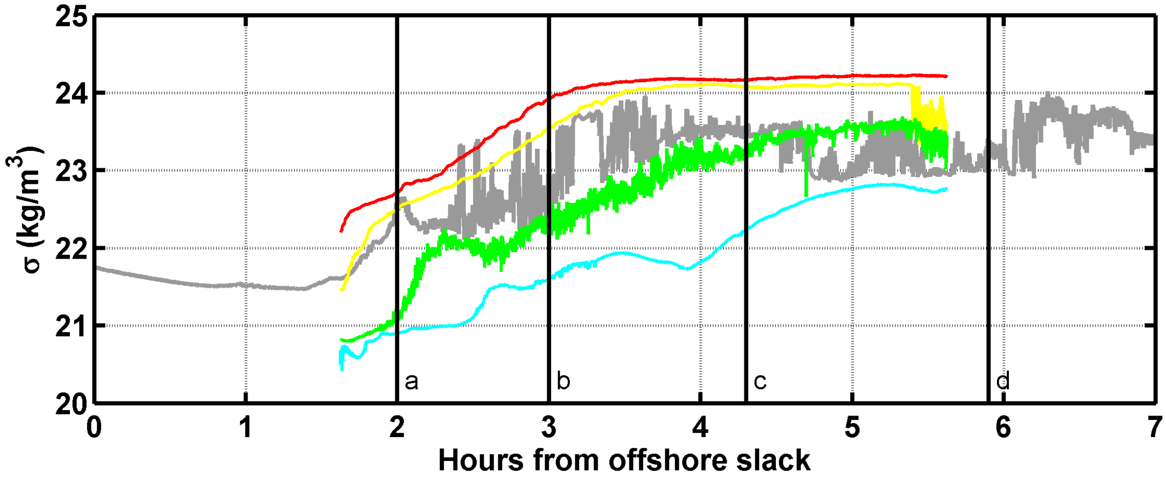

Figure 20. Time series plots of density anomaly using CTD mounted under mini-cats at ~0.5m below the surface. Colors correspond to instruments labeled in Figure 15 (**M131**, **M132**, **M083**, **M133**, **M134**). Vertical black lines correspond to time intervals depicted in Figure 23. Times are normalized to the slack (zero up-crossing) of the detrended offshore elevations from Figure 16.

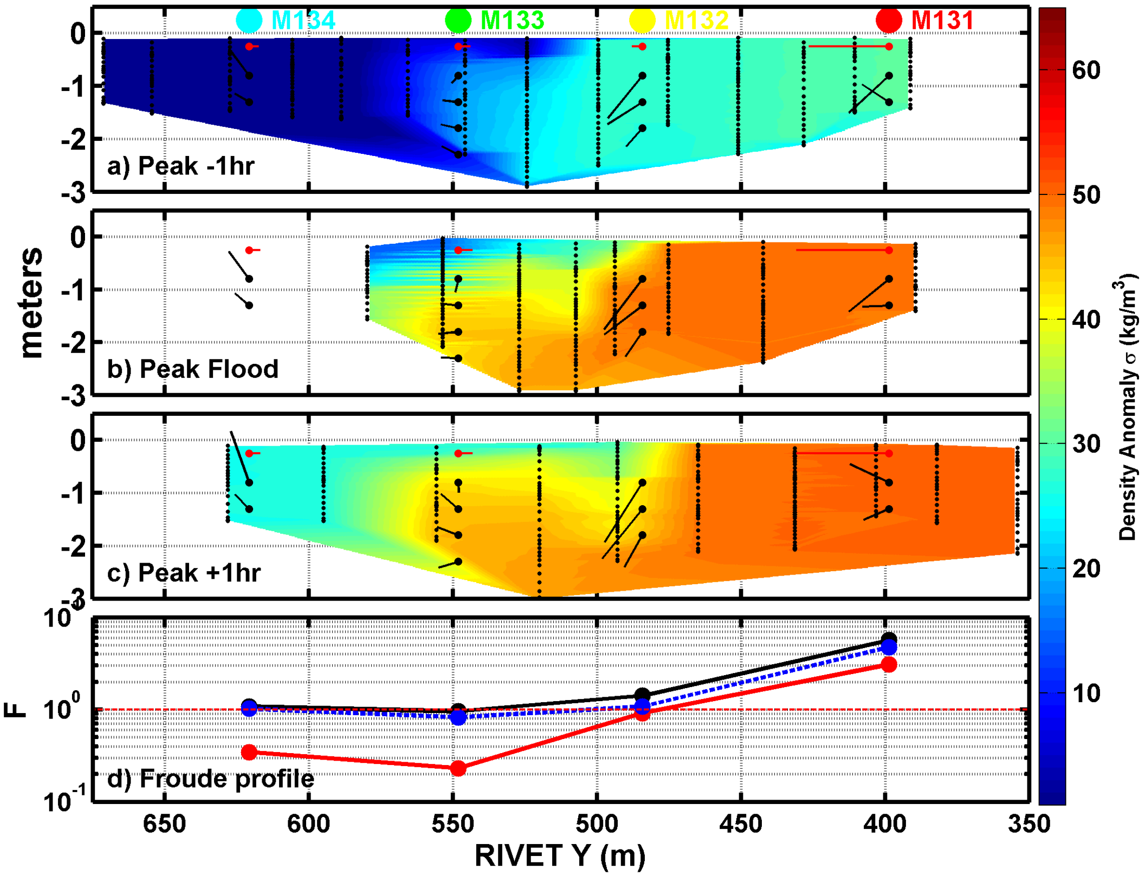

Figure 21. Cross-sections of the front on May 13 **(a)** one hour prior, **(b)** near, and **(c)** one hour following offshore high tide, which roughly corresponds to local peak flood. Coloration is density anomaly, linearly interpolated between CTD casts shown as vertical black lines. Black vectors are ADCP velocity profiles at the mini-cat locations shown. Red vectors are cross-front drifter velocities. **(d)** Froude number calculations at each mini-cat location, corresponding to the time of panel (c). Data points are calculated from total (F_t ●), cross-front (F_x ●) and along-front (F_l ●) vectors.

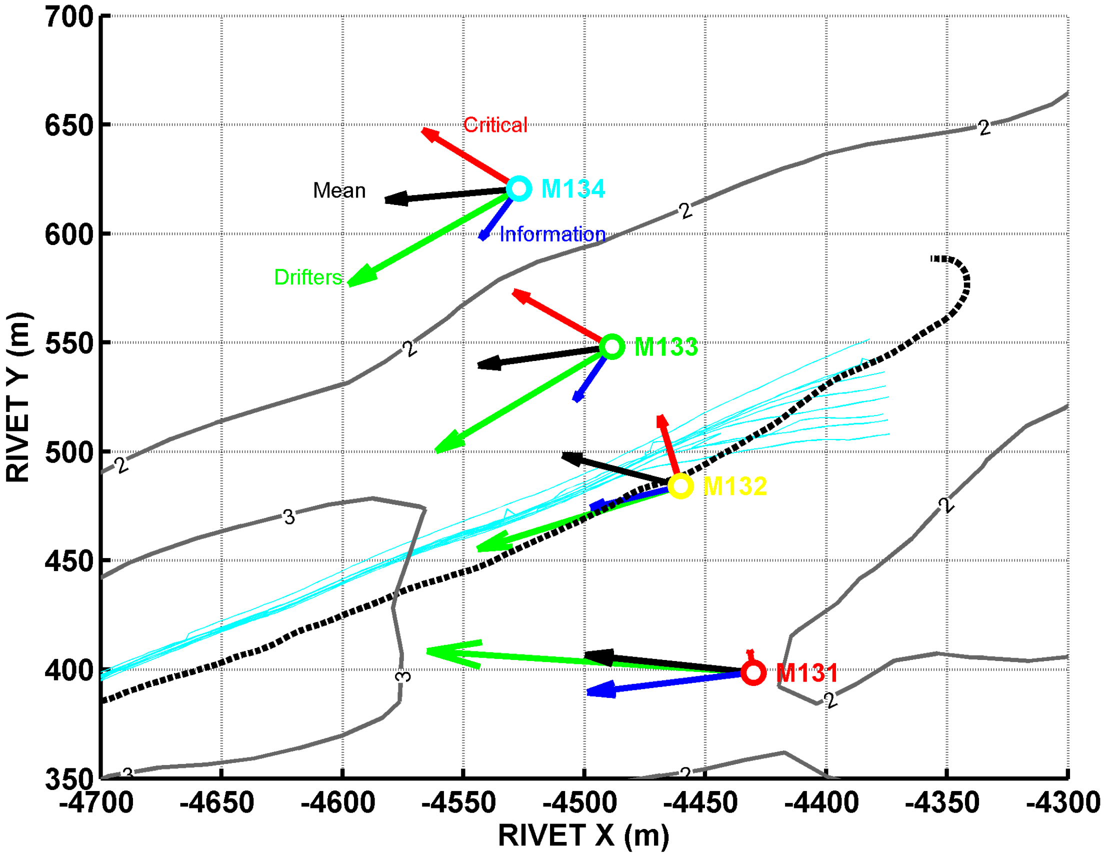

Figure 22. Mean velocity vectors (subsurface **ADCP** and surface **drifters**) and rotated components (**critical** and **information**). Dashed black line shows the GPS track of the visual small boat trace of the front on 09 May. Cyan lines show the drifter traces from the deployment set closest to the observed front on 13 May. Gray contours are labeled in meters.

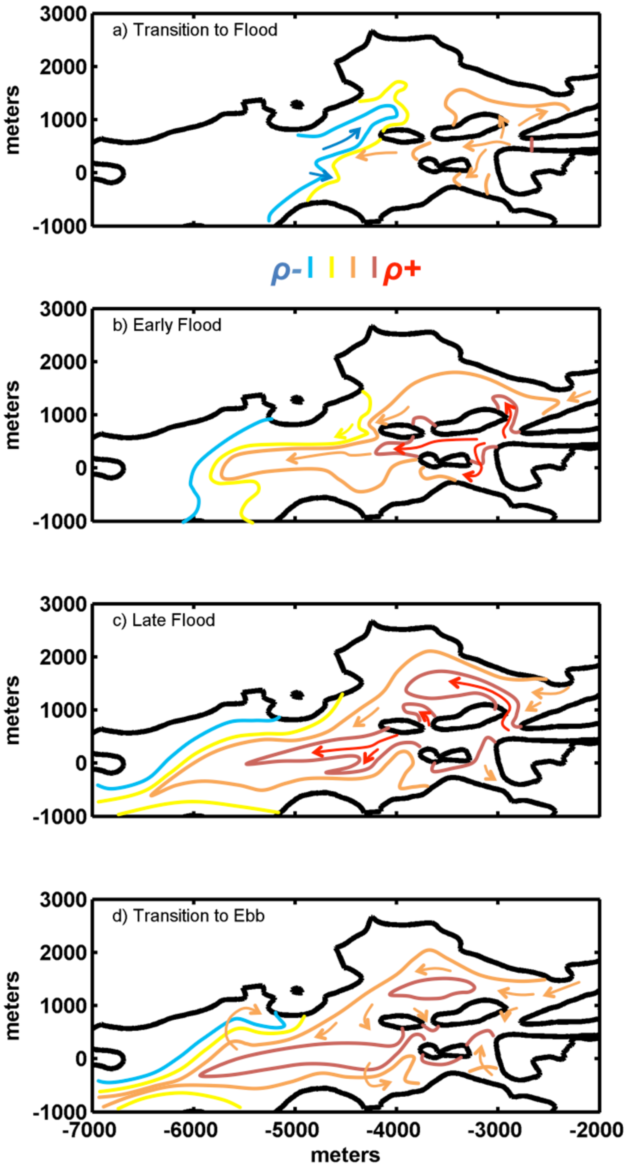

Figure 23. Sketch of proposed mixing and frontogenesis mechanisms. Thick black lines are coastlines. Colored lines are representative density contours based on model results and supported (where applicable) by the data presented in this paper. *End of ebb* (not shown): mid-density water throughout the flood delta region. Low-density water approaches front region and entering Traps Bay. **(a)** *Transition to flood*: flows turn landward in the main channel before those in the Traps Bay exit region, generating convergent shear and enhanced density gradients over the shoal. **(b)** *Early flood*: oceanic water enters main channel and splits into Traps Bay. Traps Bay exit flow turns to flood. **(c)** *Late flood*: oceanic water in main channel reaches front region. ICW flow from the north cuts off oceanic input to Traps Bay. **(d)** *Transition to ebb*: Mid-density water from ICW enters Traps Bay, while exit flow pushes density gradients southward as it turns to ebb.

THIS PAGE INTENTIONALLY LEFT BLANK

LIST OF REFERENCES

Armi, L., and D. M. Farmer (1986), Maximal two-layer exchange through a contraction with barotropic net flow, *J. Fluid Mech., 164*, 27–51.

Dame, R., M. Alber, D. Allen, M. Mallin, C. Montague, A. Lewitus, A. Chalmers, R. Gardner, C. Gilman, B. Kjerfve, J. Pinckney, and N. Smith (2000), Estuaries of the south Atlantic coast of North America: Their geographical signatures, *Estuaries, 23,* 793–819.

Deltares (2010), Delft3D-FLOW: Simulation of multi-dimensional hydrodynamic flows and transport phenomena, including sediments—User Manual, version: 3.14, revision 11214, Deltares, Delft, Netherlands.

Ensign, S.H., J.N. Halls, and M.A. Mallin (2004), Application of digital bathymetry data in an analysis of flushing times of two large estuaries, *Computers & Geosciences, 30,* 501–511, doi: 10.1016/j.cageo.2004.03.015.

Farmer, D.M., and L. Armi (1986), Maximal two-layer exchange over a sill and through the combination of a sill and contraction with net barotropic flow, *J. Fluid Mech., 164,* 53–76.

Friedrichs, C.T. (2010), Barotropic tides in channelized estuaries, in *Contemporary Issues in Estuarine Physics*, edited by A. Valle-Levinson, pp. 27-61, Cambridge University Press, New York.

Garvine, R. W. (1982), A steady state model for buoyant surface plume hydrodynamics in coastal waters, *Tellus, 34*, 293–306.

Geyer, W.R, and R.P. Signell (1992), A reassessment of the role of tidal dispersion in estuaries and bays, *Estuaries, 15,* 97–108.

Gritsenko, V.A. and I.P. Chubarenko (2010), On features of structure of bottom gravity current frontal zone, *Oceanology, 50*, 28–35, doi: 10.1134/S0001437010010030.

Haller, G. (2001), Distinguished material surfaces and coherent structures in three-dimensional fluid flows, *Physica D, 149*, 248–277.

Hansen, D.V. and M. Rattray (1966), New dimensions in estuary classification, *Limnology and Oceanography, 11*(3), 319–326.

Hench, J.L., and R.A. Luettich (2003), Transient tidal circulation and momentum balances at a shallow inlet, *J. Phys. Oc., 33*, 913–932.

Hsu, Y. L., J. D. Dykes, and R. A. Allard (2008), Validation test report for Delft3D, Rep. NRL/MR/7320–08–9079, Oceanogr. Div., Nav. Res. Lab., Stennis Space Center, Miss.

Keulegan, G.H. (1967), Tidal flow in entrances water-level fluctuation of basins in communications with seas, *Committee on Tidal Hydraulics, Tech. Bull. no. 14*, U.S. Army Engineer Waterways Experiment Station, Vicksburg, Miss.

King, D.B. (1974), The dynamics of inlets and bays, *Tech. Rep. no. 2*, Coastal and Oceanographic Engineering Laboratory, University of Florida, Gainesville.

Kjerfve, B. (1986), Comparative oceanography of coastal lagoons, in Estuarine Variability, edited by Wolfe, D.A., pp 63-81, Academic, San Diego, Calif.

Koroknay, B.J. (2012), Quantifying watershed loads to a low-relief coastal plain estuary: the New River Estuary, NC, School of Marine Science, College of William and Mary, Williamsburg, Va.

Largier, J.L. (1992), Tidal intrusion fronts, *Estuaries, 15*, 26–39.

Lesser, G. R., J. A. Roelvink, J. A. T. M. Van Kester, and G. S. Stelling (2004), Development and validation of a three-dimensional morphological model, *Coastal Eng., 51,* 883–915, doi:10.1016/j.coastaleng.2004.07.014.

Li, C (2002), Axial convergence fronts in a barotropic tidal inlet – sand shoal inlet, VA, *Cont. Shelf Res., 22*, 2633–2653.

Lowe, J.L., P.F. Linden, and J.W. Rottman (2002), A laboratory study of the velocity structure in an intrusive gravity current, *J. Fluid Mech., 456,* 33–48, doi: 10.1017/S0022112001007303.

MacDonald, D.G. and W.R. Geyer (2005), Hydraulic control of a highly stratified estuarine front, *J. Phys. Oc., 35*, 374-387.

Marmorino, G.O., C.L. Trump (1996), High-resolution measurements made across a tidal intrusion front, *J. Geophys. Res., 101,* 25,661-25,674.

Morris, B. J. (2001), Nearshore wave and current dynamics, PhD thesis, Nav. Post Grad. Sch., Monterey, Calif.

Mulligan, R. P., A. E. Hay, and A. J. Bowen (2008), Wave-driven circulation in a coastal bay during the landfall of a hurricane, *J. Geophys. Res., 113,* C05026, doi:10.1029/2007JC004500.

Mulligan, R. P., A. E. Hay, and A. J. Bowen (2010), A wave-driven jet over a rocky shoal, *J. Geophys. Res., 115,* C10038, doi:10.1029/2009JC006027.

Mulligan, R. P., W. Perrie, and S. Solomon (2011), Dynamics of the Mackenzie River plume on the inner Beaufort Shelf during an open water period in summer, *Estuarine Coastal Shelf Sci., 89,* 214–220, doi:10.1016/j.ecss.2010.06.010.

Nunes, R.A. and J.H. Simpson (1985), Axial convergence in an well-mixed estuary, *Estuarine, Coastal and Shelf Science, 20*, 637-649.

O'Donnell, J., (1990), The formation and fate of a river plume: A numerical model, *J. Phys. Oceanogr., 20,* 551–569.

O'Donnell, J., and R. W. Garvine (1983), A time dependent two-layer model of buoyant plume dynamics, *Tellus, 35A,* 73–80.

O'Donnell, J., S.G. Ackleson, and E.R. Levine (2008), On the spatial scales of a river plume, *J. Geophys. Res., 113*, C04017. doi:10.1029/2007JC004440.

Pawlowicz R., B. Beardsley, and S. Lentz (2002), Classical tidal harmonic analysis including error estimates in MATLAB using T_TIDE, *Comput. Geosci., 28*, 929-28,937.

Peikert, R. and F. Sadlo (2010), Topology-guided visualization of constrained vector fields, in *Topology-based methods in visualization (mathematics and visualization)*, edited by H. Hauser, H. Hagen and H. Theisel, pp. 21-34, Springer.

Pratt, L.J. (2008), Critical conditions and composite Froude numbers for layered flow with transverse variations in velocity, *J. Fluid Mech., 605*, 281–291, doi:10.1017/S002211200800150X.

Ralston, D.K., W.R. Geyer, J.A. Lerczak (2010), Structure, variability, and salt flux in a strongly forced salt wedge estuary*, J. Geophys. Res., 115,* C06005.

Ralston, D. K., W. R. Geyer, and J. C. Warner (2012), Bathymetric controls on sediment transport in the Hudson River estuary: Lateral asymmetry and frontal trapping, *J. Geophys. Res., 117,* C10013, doi:10.1029/2012JC008124.

Reniers, A.J.H.M., J.H. MacMahan, E.B. Thornton, T.P. Stanton, M. Henriquez, J.W. Brown, J.A. Brown, and E. Gallagher (2009), Surf zone surface retention on a rip-channeled beach, *J. Geophys. Res., 114*, C10010, doi: 10.1029/2008JC005153.

Roelvink, J.A. and A.J.H.M. Reniers (2011), A Guide to Modeling Coastal Morphology, *Advances in Coastal and Ocean Engineering, vol. 12*, World Scientific, Hackensack, NJ.

Ryscavage, J.M. (2010), Surf City and North Topsail Beach, NC, final feasibility report and environmental impact statement, U.S. Army Corps of Engineers, Wilmington, NC.

Sheets, J. (2013), Salinity, temperature, and optical characterization of a tidally choked estuary connected to two contrasting intra-coastal waterways, M.S. thesis, Oceanography Department, Naval Postgraduate School, Monterey, Calif.

Simpson, J.H., J. Brown, J. Matthews, and G. Allen (1990), Tidal straining, density currents, and stirring in the control of estuarine stratification, *Estuaries, 13*, 125–132.

Stommel, H. M. & Farmer, H. G. (1952), Abrupt change in width in two-layer open channel flow, J. Marine Res., 11, 205–214.

Talke, S.A., A. R. Horner-Devine, and C. C. Chickadel (2010), Mixing layer dynamics in separated flow over an estuarine sill with variable stratification, *J. Geophys. Res., 115*, C09004, doi:10.1029/2009JC005467.

Thain, R.H., A.D. Priestley and M.A. Davidson (2004), The formation of a tidal intrusion front at the mouth of a macrotidal, partially mixed estuary: a field study of the Dart estuary, UK, *Estuarine, Coastal and Shelf Science, 61*, 161-172, doi:10.1016/j.ecss.2004.04.012.

Valle-Levinson, A., W.C. Boicourt, and M.R. Roman (2003), On the linkages among density, flow, and bathymetry gradients at the entrance to the Chesapeake Bay, *Estuaries, 26*, 1437-1449.

INITIAL DISTRIBUTION LIST

1. Defense Technical Information Center
   Ft. Belvoir, Virginia

2. Dudley Knox Library
   Naval Postgraduate School
   Monterey, California